Inertial and Aerodynamic Tail Steering of a Meso-scale Legged Robot

by

Nicholas Joseph Kohut

A dissertation submitted in partial satisfaction of the
requirements for the degree of
Doctor of Philosophy

in

Engineering - Mechanical Engineering

in the

Graduate Division

of the

University of California, Berkeley

Committee in charge:

Professor Ronald S. Fearing, Chair
Professor Oliver M. O'Reilly, Co-Chair
Professor J. Karl Hedrick
Professor Robert J. Full

Spring 2013

Inertial and Aerodynamic Tail Steering of a Meso-scale Legged Robot

Abstract

Inertial and Aerodynamic Tail Steering of a Meso-scale Legged Robot

by

Nicholas Joseph Kohut

Doctor of Philosophy in Engineering - Mechanical Engineering

University of California, Berkeley

Professor Ronald S. Fearing, Chair

Legged robots have excellent potential for all-terrain mobility, and are capable of many behaviors wheeled and tracked robots are unable to perform. However, legged robots have difficulty turning rapidly, or turning while running forward. For maximum maneuverability, terrestrial robots need to be able to turn precisely, quickly, and with a small radius. Previous efforts at turning in legged robots primarily have used leg force or velocity modulation. This work presents two novel methods of legged robot turning.

The first of these methods is inertial tail turning, or using a rapidly actuated, weighted tail to cause a sudden change in angular momentum, turning the body of the robot. The tailed robot presented here is able to make rapid, precise turns. By rapidly rotating the tail as the robot runs forward, the robot was able to make sudden 90° turns at 360 $^\circ sec^{-1}$, making it the fastest turning legged robot known to the author at the time of this publication. Unlike other turning methods, this turn is performed with almost no change in forward running speed. The dynamics of this maneuver have also been modeled, to examine how features, such as tail length and mass, affect the robot's turning ability. This approach has produced turns with a radius of 0.4 body lengths at 3.2 body lengths per second running speed. Using a nonlinear feedback controller, turns with an accuracy of ± 5° for a 60° turn have been achieved.

The second method of turning presented here allows a legged robot to turn continuously while running at high speeds. This remains a difficult task for legged robots, but is crucial for maneuvering quickly in a real-world environment. SailRoACH is the first running robot that uses aerodynamic forces to turn. A flat plate serves as an aerodynamic surface, and depending on its position, can be used to impart positive or negative aerodynamic yaw torques on the robot as it runs forward, causing turns of up to $70^\circ sec^{-1}$ at a radius of 1.2 meters and a running speed of 1.8 ms^{-1}. A scale analysis of aerodynamic steering is also presented, showing this method is most effective for small robots. Comparisons to other steering methods are made, showing that inertial and aerodynamic steering are superior for high speed turns at high forward velocity, compared to existing methods.

Dedicated to my father, George Kohut, Ph. D. His hard work and perseverance inspire me to be a good man, and to tackle life's difficult challenges, both professional and personal.

Contents

List of Figures

List of Tables

Acknowledgments

It would be impossible to write a complete acknowledgements section for this work, as so many people have influenced me in my six years at Berkeley. As such, an incomplete acknowledgement section will have to suffice. I would like to thank Professor Ronald Fearing, my advisor and mentor, for all the time he has dedicated to my work and me, and for taking on a student who wanted to join an experimental robotics lab but did not know how to solder. I would also like to thank Professors Robert Full, Karl Hedrick, Oliver O'Reilly, Andrew Packard, Francesco Borrelli and Ming Gu for their guidance and mentorship.

Members of the Biomimetic Millisystems Laboratory, both past and present, have been essential to this achievement, including but not limited to, Aaron Hoover, Andrew Pullin, David Zarrouk, Kevin Peterson, Andrew Gillies, Paul Birkmeyer, and Duncan Haldane. Many peers have also had a profound effect on me in my time here, both as an engineer and a person. Those include Andy Hurwich, Selina Pan, Tony Ho, Mary Phillips, Vera Dadok, Josh Mackanic, Joanna Bechtel, Russell Muren, Moneer Helu, Rabia Chaudhry, Katie Strausser, and Samveg Saxena.

Of course, my parents George and Jacquelyn have been an incredible source of support for me, and I could not have done this without them. Finally, I would like to acknowledge my fiancée Katherine, for always being by my side when needed, and always understanding that even when I had to work through the weekend, she was still the most important thing in my life.

Figure 0.1: Biomimetic Millisystems Laboratory, October 2012.

Chapter 1

Introduction

1.1 Context and Motivation

Currently legged robots have difficulty running and turning simultaneously at high speeds. Animals are able to employ numerous actuators per leg, allowing them to maintain high speeds and coordinate leg forces to effect a turn. Robots are often limited to one actuator per leg or have a single actuator for several legs. This makes sophisticated coordination of leg forces to produce high running speeds and turns simultaneously difficult. This work seeks to find a solution to this problem by separating the legs from generating the turning moment. By using a single additional actuator, a turning moment can be applied through rapidly moving an inertial element, causing a turn. This allows leg forces to stay coordinated and decouples forward motion and turning. Turning by aerodynamic torques has a similar effect.

1.2 Overview

This chapter discusses the context and motivation for inertial and aerodynamic tail steering on legged robots, and discusses the contributions to the field of robotics found in this body of work. Chapter 2 discusses current and past approaches to legged robot maneuverability, while also examining maneuverability solutions employed by animals. Biological and artificial methods of turning and/or use of tails are examined, as are the use of passive aerodynamics in running robots. Finally, Chapter 2 reviews the RoACH (Robotic Autonomous Crawling Hexapod) family of robots, of which TAYLRoACH and SailRoACH, the two robots detailed in this dissertation, are a part.

Chapter 3 details modeling and simulation of the inertial and aerodynamic turning methods. Models are developed from first principles for inertial turning, while empirical models are used for friction, motor torque, and aerodynamic torque. This chapter also presents physical verification of these models. Chapter 4 details the mechanical design of the three tail mechanisms used for experimental results. It also details the software and control laws used in tail operation, and provides a brief analysis of gear ratio selection.

Chapter 5 reports the experimental results, including inertial turning open loop response, inertial turning closed loop response using a nonlinear controller, and aerodynamic turning. The performance of the closed loop controller is examined, and inertial and aerodynamic steering are compared to other legged robot steering solutions.

Chapter 6 serves as a conclusion to the dissertation, summarizes the work and contributions, and provides a possible scope of future work.

1.3 Contributions

This work makes both theoretical and technological contributions to the field of robotics. Theoretical contributions include a planar dynamic model of inertial turning that incorporates friction and an empirical motor model. It is shown that this model can be used to inform the design of an inertial tail system. A theoretical comparison of best case inertial and legged turning methods is made, showing that inertial turning is preferable for low friction surfaces, while legged turning may be more effective on high friction surfaces. A discussion of scale effects for inertial, aerodynamic, and differential drive steering is also made.

Experimental contributions include the first demonstration of terrestrial inertial turning on a legged robot. This turning is highly rapid, inducing turns up to $400^\circ sec^{-1}$, making TAYLRoACH the fastest turning legged robot known to the author. A nonlinear controller was developed showing that this method of turning could be precise with feedback, and its performance has been characterized. Additionally, the first use of passive aerodynamics to induce a turn in a legged robot is demonstrated. Finally, it is shown that both inertial and aerodynamic tail steering have significant advantages for turning while running at high speeds when compared to other turning methods.

Chapter 2

Legged Robot Maneuverability

2.1 Background

The capability of a mobile robot can be though of as a product of its mobility, intelligence, and quantity [9]. Small legged robots, due to their low size and packaging constraints, often do not possess great intelligence as an individual unit. However, due to their generally low cost and ease of fabrication, they can be built in large numbers and have high multiplicity. This means that if a small legged robot can achieve high mobility, its capability can be very high, exceeding that of larger, more expensive, more complex robots.

$$(mobility)(intelligence)(quantity) = capability \tag{2.1}$$

Mobility comes in many forms and can be achieved in a variety of terrains and media. Generally, animals and robots are specialists in ground, air, or water locomotion. Few are able to excel in all three of these domains. For example, the ostrich is able to cover ground at over 40 mph [6] but does not fly. The hummingbird, relatively closely related to the ostrich, can execute remarkable aerial maneuvers but is unable to walk [15].

Here the focus is on ground mobility. Ground mobility can be expressed as the ability to navigate various types of terrains, at various speeds. Also important to mobility is the ability to turn. Without the ability to make rapid, precise turns, many animals would go hungry (in the case of predators) or be an easy meal (in the case of prey). While robots do not (as of this writing) need to consume other robots for energy, they are often tasked with missions that require excellent ground mobility and exceptional turning. In a search and rescue situation, depicted in Fig. 2.1, the ability to turn quickly and in small spaces could be the difference between life and death. Similarly, if an area must be searched quickly to determine if there are any harmful substances, rapid turning can help a robot cover the same ground in less time. In this work I show how the addition of a tail can greatly increase a legged robot's ground mobility by improving its ability to turn.

2.2 Animals and Robots use of Tails

In the animal kingdom, tails are used for many purposes, from fat storage [41] to communication [38]. Animals also use their tails to increase their maneuverability. Geckos are able to right themselves from a fall within 106 ± 6 msec using their tail [19], shown in Fig. 2.2. The Rightbot robot [20] is able to mimic this behavior as well. Similarly, *Agama agama* lizards have been shown to be able to control the pitch angle of their body by modulating the position of their tails while airborne [29]. This allows the lizard to respond to a disturbance just before or after a jump, and land appropriately. Tailbot [4] was built to replicate this behavior, and can drive off of ramped jumps, then adjust its tail to counteract any tumbling that would otherwise occur. This behavior is shown in Fig. 2.3. This principle was shown to apply in larger robots as well, when similar behavior was implemented on an RHex-class robot [18].

Tails can also be used to control the yaw attitude of an animal or robot. Using a vertical wind tunnel, Jusufi et. al [19] showed that lizards can control their yaw orientation while airborne.

Figure 2.1: A robot with excellent ground mobility could navigate a collapsed building, reaching places humans could not.

This could be useful for control during gliding. It has recently been shown that when *agama* lizards turn, 57% of the body rotation in the first leg stride can be attributed to the motion of the tail, with the rest of the turn being caused by ground reaction forces from the legs of the animal [28]. The TAYLRoACH robot presented in this dissertation mimics this behavior, though for most experiments turns are produced by the tail only. Aerial animals [8] and robots [34] also use tails to affect the angular momentum of their body.

Robots find many other uses for tails that can be beneficial. Many climbing robots use tails to provide normal force against the climbing surface [40][21][22][30]. This produces an anti-peeling moment, and also may serve to lower the center of gravity of the robot beneath the center of adhesion, aiding in stability. ROCR (shown in Fig. 2.4) is a climbing robot that "uses an actuated tail to propel itself upward" [36]. Aquatic robots may produce turns with tails by exploiting hydrodynamic forces [11].

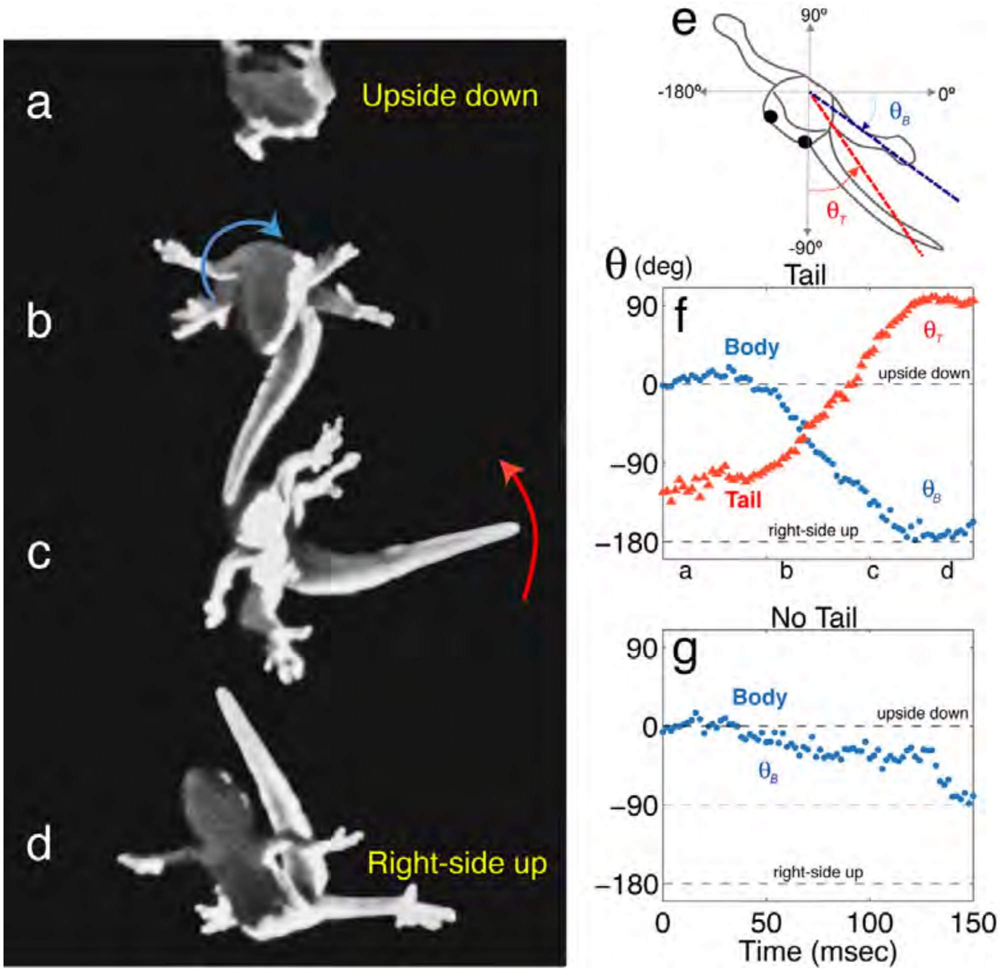

Figure 2.2: A gecko uses its tail to right itself during a fall. Figure courtesy of Ardian Jusufi, used with permission.

2.3 Animals and Robots Turning

Turning is an essential aspect of maneuverability. Animals and robots find many solutions to the problem of turning. As mentioned above, animals and robots may use their tails to produce turns, either through an exchange of angular momentum or the use of hydrodynamic forces.

One way to perform a turn is through kinematics. In a legged robot or animal, this can be done either by using longer strides with the outer legs and shorter strides with the inner legs, or by moving the outer legs faster than the inner legs. The stick insect changes its stride length to produce a turn [7], as do mice [43], and the robot Hector [39]. The OctoRoACH robot [37] varies its stride frequency of one side relative to the other to produce a turn. For kinematic turns, enough friction must be present to enforce a sticking condition on the legs. Otherwise slip will occur and

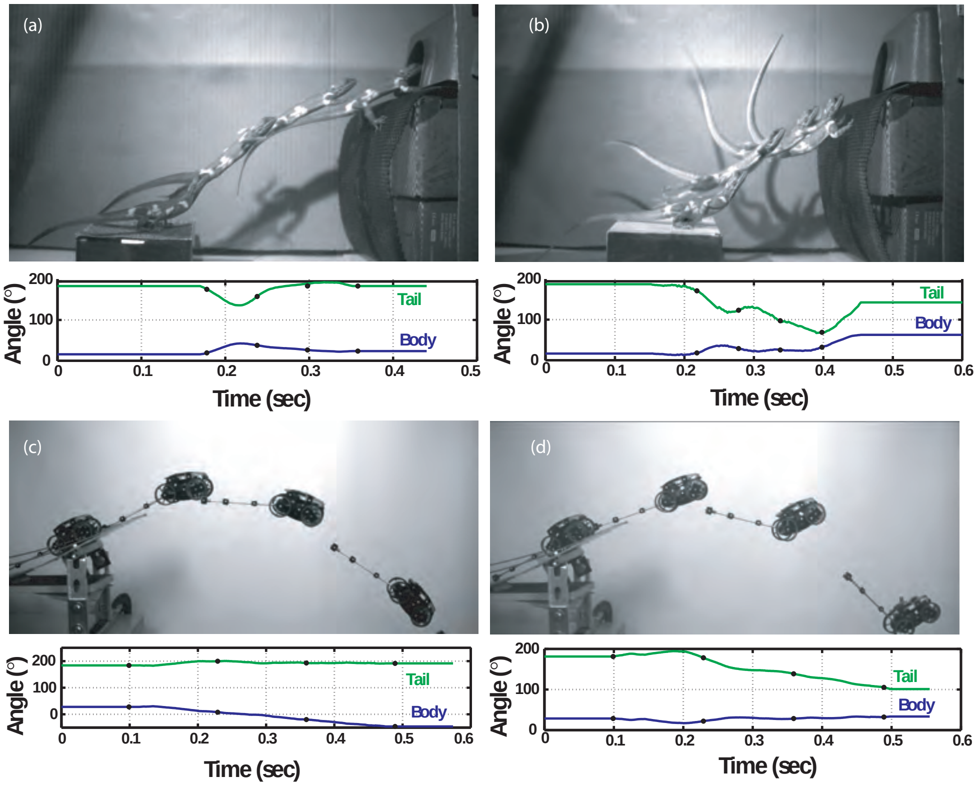

Figure 2.3: (a) Agama lizard jumping off high traction obstacle, allowing tail and body angles to remain constant. (b) A low traction vault surface produces an angular momentum perturbation. By swinging their tail upwards, lizards redirected angular momentum from the body into the tail to maintain body angle. (c, d) A robot drives off a ramp, producing a nose-down perturbation in body angular momentum. (c) Without PD feedback control, the body and tail rotate as a rigid body. (d) With PD feedback control, the tail swings upwards to stabilize the body and keep the body angle constant. Figure and caption courtesy of Tom Libby, used with permission. Originally published in [29].

the turn may not be executed.

Turns can also be generated dynamically, by using ground reaction forces to produce a turning moment. Cockroaches use this method [17], as does the SPRAWL family of robots [31]. This can produce very rapid turns, up to 230 $^\circ sec^{-1}$in the iSprawl robot. These turns can be generated with the legs sticking or slipping, and are generally limited by the available traction. One innovative, dynamic method of turning involves changing the center of mass location of a wheeled vehicle, thus altering the normal forces on the wheels, which changes the lateral forces at the tires and produces a turn [32].

There are many other ways to turn, though most of these can be reduced to the kinematic or

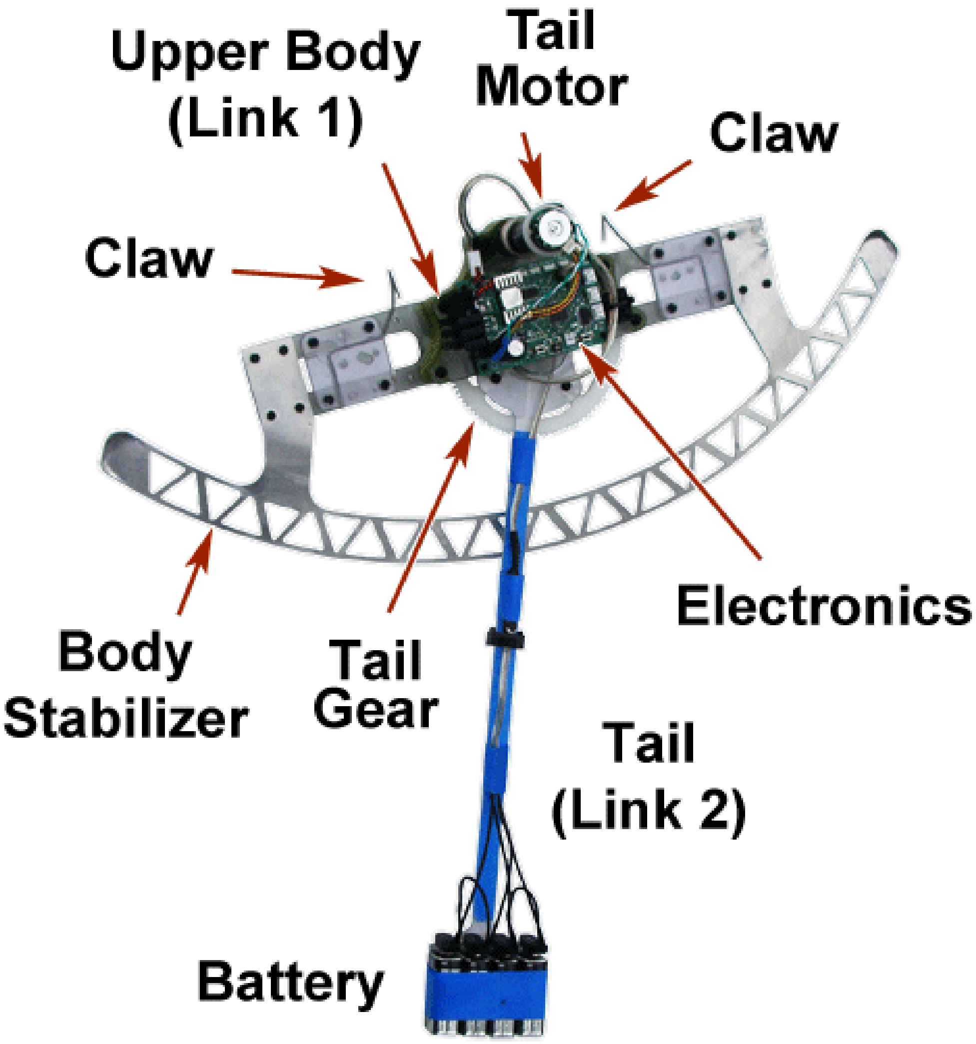

Figure 2.4: ROCR uses an actuated tail to move its body and climb upwards. Figure courtesy of Will Provancher, used with permission.

dynamic case. RHex alters the amount of time each leg is on the ground while keeping the overall leg frequency constant [33]. Differential leg stiffness is used by the DynaRoACH robot to induce turning [14], while the miniRoACH robot modulates actuation timing to turn [13]. The DASH robot can produce turns by warping its compliant body, thus altering its running kinematics, as shown in Fig. 2.6 [2].

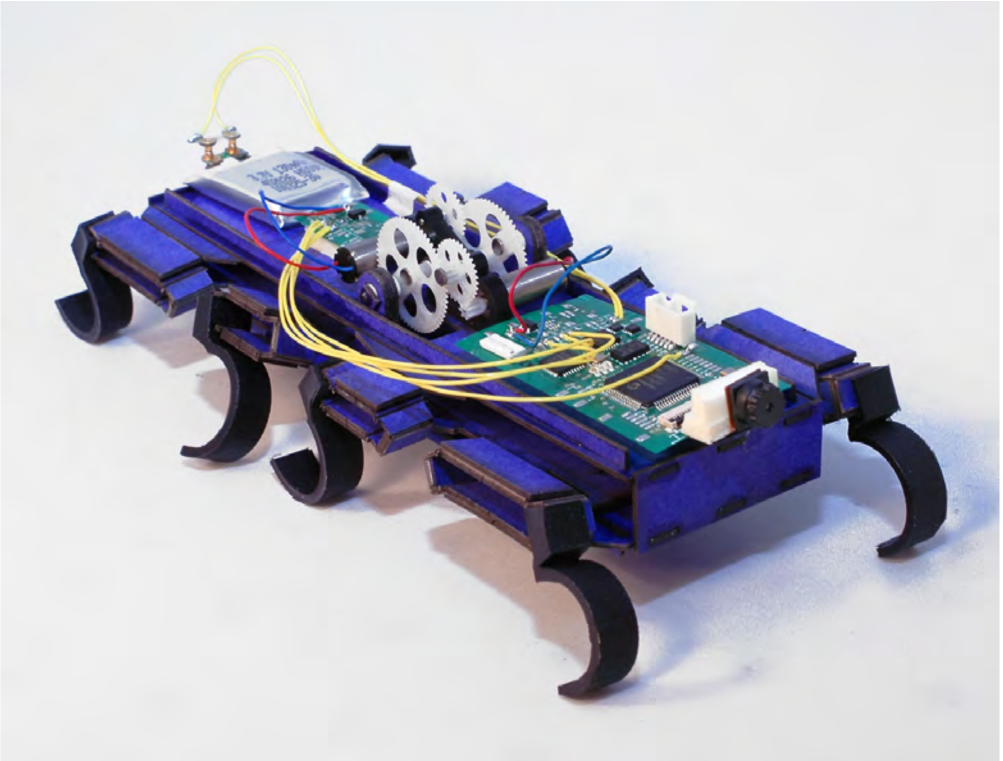

Figure 2.5: The OctoRoACH robot uses differential speed drive of its legs to produce a turn. Figure courtesy of Andrew Pullin. Used with permission.

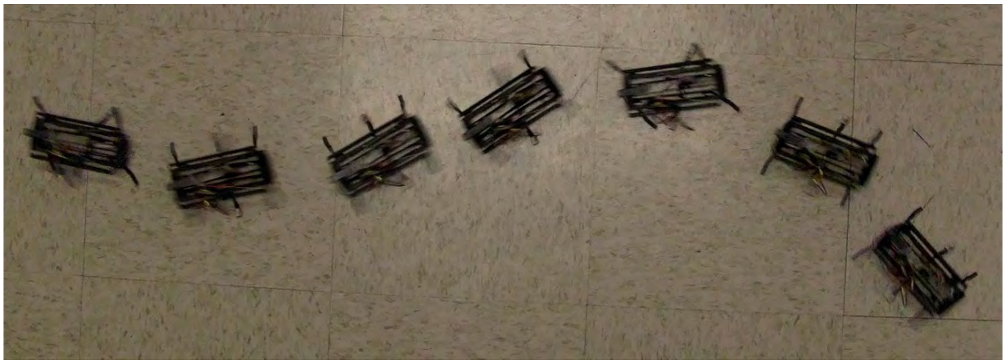

Figure 2.6: DASH can warp its body kinematics, changing its leg stroke, and inducing a turn. Figure courtesy of Paul Birkmeyer, used with permission.

2.4 Legged Robots Use of Aerodynamics

Aerodynamics are a relatively unexplored realm for turning in running robots, although they have been used for other functions.

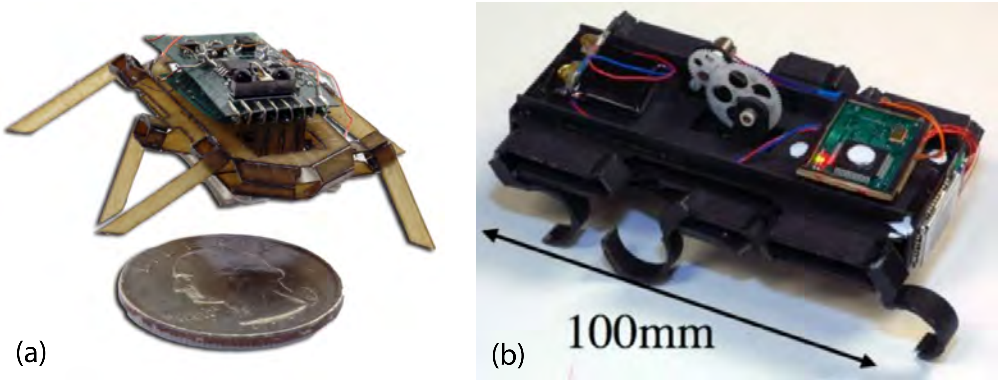

Figure 2.7: (a) RoACH was first in the RoACH family of robots. At the time of its design, it was the world's smallest walking robot. (b) DynaRoACH is a minimally actuated legged robot, that is the predecessor of the OctoRoACH and TAYLRoACH. Images courtesy of Aaron Hoover. Used with permission.

Aerodynamics are of course a crucial aspect of flying robots [27][45][42]. Other non-flying robots have exploited aerodynamics for a performance advantage. DASH+Wings [35] showed improved performance in forward running speed and stability compared to its wingless version, while the EPFL jumpglider [26] also employs aerodynamics to increase its mobility. Little work has been done however, on aerodynamic surfaces in running robots used for purposes other than flight or gliding. The VelociRoACH [10], is a notable exception, and uses a large roll stabilizer with aerodynamic damping to increase its stability while running at high speeds. To the author's knowledge, steering of a legged robot using aerodynamic forces while the robot runs over the ground has not been explored.

2.5 Overview of previous RoACH Robots

TAYLRoACH is an evolution of several years of Scaled Composite Microstructures [12] robots. The first legged robot built using SCM was the RoACH [13], or Robotic Autonomus Crawling Hexapod. RoACH weighed 2.4 grams and could walk forward and turn.

DynaRoACH was a palm-sized evolution of the smaller RoACH. These robots are shown in Fig. 2.7. DynaRoACH is dynamically tuned for high-speed running and can travel at 1.4 m/s [14]. DynaRoACH is minimally actuated and featured a single DC motor to drive all 6 legs. To facilitate better turning, the OctoRoACH was designed [37]. The OctoRoACH features two DC motors, one driving the left set of legs while the other driving the right set. The VelociRoACH (from which TAYLRoACH is most directly derived) also uses this configuration. VelociRoACH incorporates design elements from DASH [2] and CLASH [1] and has been tuned for high speed running, reaching 2.7 m/s [10].

Chapter 3

Modeling and Simulation

3.1 Background

This chapter examines a planar mechanics model, coupled with a motor model and simple friction model, to predict the performance of an inertial tail for turning. Model sensitivity analysis is performed to inform the design of the TAYLRoACH robot. An empirical aerodynamic model is also presented, which is used to inform the operating parameters of the SailRoACH robot. The effect of scale is discussed for both inertial and aerodynamic sail turning. Finally, physical verification of the models is presented.

3.2 Mechanics Model

To model the turning of TAYLRoACH, we consider a point mass m_t on a massless rod of length ℓ representing the tail, and a rigid body with mass m_b and yaw inertia I_b representing the robot body, as seen in Figure 3.1. The location where the tail is mounted to the body is referred to as the pin. Only planar dynamics are considered.

The robot has width $2a$ and length $2b$. The body's yaw angle relative to the world frame is θ. The tail's yaw angle relative to the world is ϕ. The angle of rotation of the body relative to the tail is

$$\psi = \theta - \phi \tag{3.1}$$

3.2.1 Balances of Angular and Linear Momenta

Rigorous analysis of tail-body dynamics while a robot is in free fall have been explored in [18, 46]. The analysis presented below is similar but incorporates friction from the legs, a tail offset from the center of mass, a piecewise linear motor model, and compares turning with the tail to legged steering, also modeled here.

We define the position vector of the center of mass of the body:

$$\mathbf{x}_b = \mathbf{r} + x\mathbf{E}_1 + y\mathbf{E}_2 \tag{3.2}$$

and the position vectors of the pin and tail are, respectively,

$$\mathbf{x}_{pin} = \mathbf{x}_b - b\mathbf{e}_2 \tag{3.3}$$

and

$$\mathbf{x}_t = \mathbf{x}_b - b\mathbf{e}_2 - \ell\mathbf{t}_2 \tag{3.4}$$

From these expressions, we find a representation for the position vector of the center of mass of the body-tail system.

$$\mathbf{r} = \frac{m_b\mathbf{x}_b + m_t\mathbf{x}_t}{m_b + m_t} \tag{3.5}$$

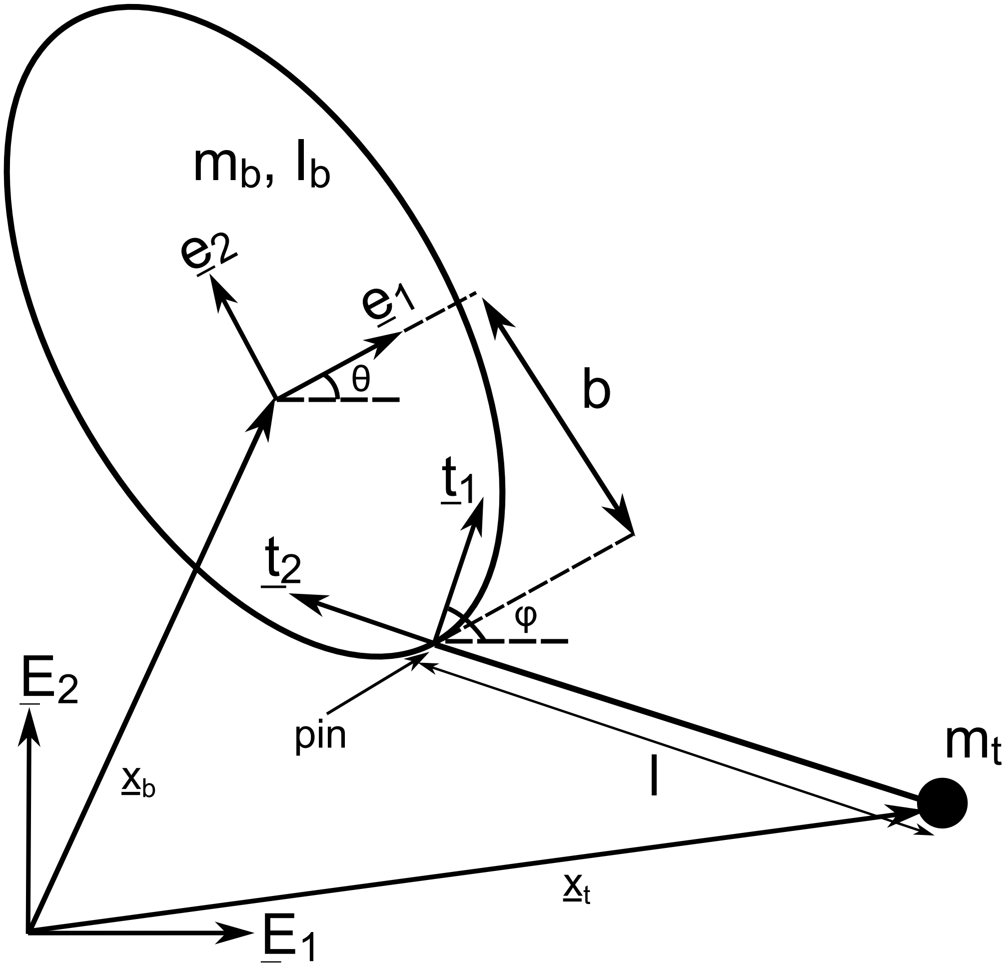

Figure 3.1: Planar model of the robot body and tail.

The position vectors of the centers of mass of the body and tail relative to the system's center of mass can be expressed as

$$\mathbf{r}_b = \mathbf{x}_b - \mathbf{r} = -\frac{m_t\,(b\sin\theta + \ell\sin\phi)}{m_b + m_t}\mathbf{E}_1 + \frac{m_t\,(b\cos\theta + \ell\cos\phi)}{m_b + m_t}\mathbf{E}_2 \tag{3.6}$$

and

$$\mathbf{r}_t = \mathbf{x}_t - \mathbf{r} = \frac{m_b\,(b\sin\theta + \ell\sin\phi)}{m_b + m_t}\mathbf{E}_1 - \frac{m_b\,(b\cos\theta + \ell\cos\phi)}{m_b + m_t}\mathbf{E}_2 \tag{3.7}$$

The angular momentum of the robot body relative to the origin is

$$\mathbf{H}_b = \mathbf{I}_b\boldsymbol{\omega}_b + m_b(\mathbf{r}_b + \mathbf{r}) \times (\mathbf{v}_b + \dot{\mathbf{r}}) \tag{3.8}$$

where $\mathbf{v}_b = \dot{\mathbf{r}}_b$ and $\boldsymbol{\omega}_b = \dot{\theta}\mathbf{E}_3$ is the angular velocity vector of the robot body. The corresponding expression for the angular momentum of the tail is

$$\mathbf{H}_t = m_t(\mathbf{r}_t + \mathbf{r}) \times (\mathbf{v}_t + \dot{\mathbf{r}}) \tag{3.9}$$

where $\mathbf{v}_t = \dot{\mathbf{r}}_t$.

We are now in a position to write down the balances of linear and angular momenta for the system and its components. First, we have the balance of linear momentum for the system:

$$(m_b + m_t)\,\ddot{\mathbf{r}} = \mathbf{F}_f \tag{3.10}$$

where $\mathbf{F}_f$ is the friction force. Next, we have the balances of angular momenta for the body and the tail

$$\dot{\mathbf{H}}_b = -\mathbf{T} + \mathbf{r}_{pin} \times \mathbf{F}_{pin} + \mathbf{M}_f \tag{3.11}$$

and

$$\dot{\mathbf{H}}_t = \mathbf{T} - \mathbf{r}_{pin} \times \mathbf{F}_{pin} \tag{3.12}$$

where $\mathbf{M}_f = M_f\mathbf{E}_3$ is the moment from friction and $\mathbf{T} = T\mathbf{E}_3$ is the tail torque.

The only external forces on the system are due to friction and normal forces. The tail torque and pin reaction forces are internal. It is assumed that the friction forces on the system form a couple, and provide no net force, but do provide a net moment. Taking a balance of linear momentum of the system, we quickly find that the velocity vector of the center of mass of the system is constant:

$$\ddot{\mathbf{r}} = \mathbf{0} \tag{3.13}$$

Without loss of generality, we can define an inertial frame attached to the center of mass of the system whose origin translates at constant velocity with the center of mass of the system:

$$\mathbf{r} = \mathbf{0} \tag{3.14}$$

Since the pin force is the only net force on the body, it can be calculated as

$$\mathbf{F}_{pin} = m_b\left(\ddot{\mathbf{r}}_b + \ddot{\mathbf{r}}\right) = m_b\ddot{\mathbf{r}}_b \tag{3.15}$$

From here, we can calculate equations of motion based on the change in angular momentum and the net moments on the tail and body:

$$\begin{bmatrix} b^2k + I_b & b\ell k\cos(\psi) \\ b\ell k\cos(\psi) & \ell^2 k \end{bmatrix} \begin{bmatrix} \ddot{\theta} \\ \ddot{\phi} \end{bmatrix} = \begin{bmatrix} -T + M_f + b\ell k\sin(\psi)\dot{\phi}^2 \\ T + b\ell k\sin(\psi)\dot{\theta}^2 \end{bmatrix} \tag{3.16}$$

where

$$k = \frac{m_b m_t}{m_b + m_t} \tag{3.17}$$

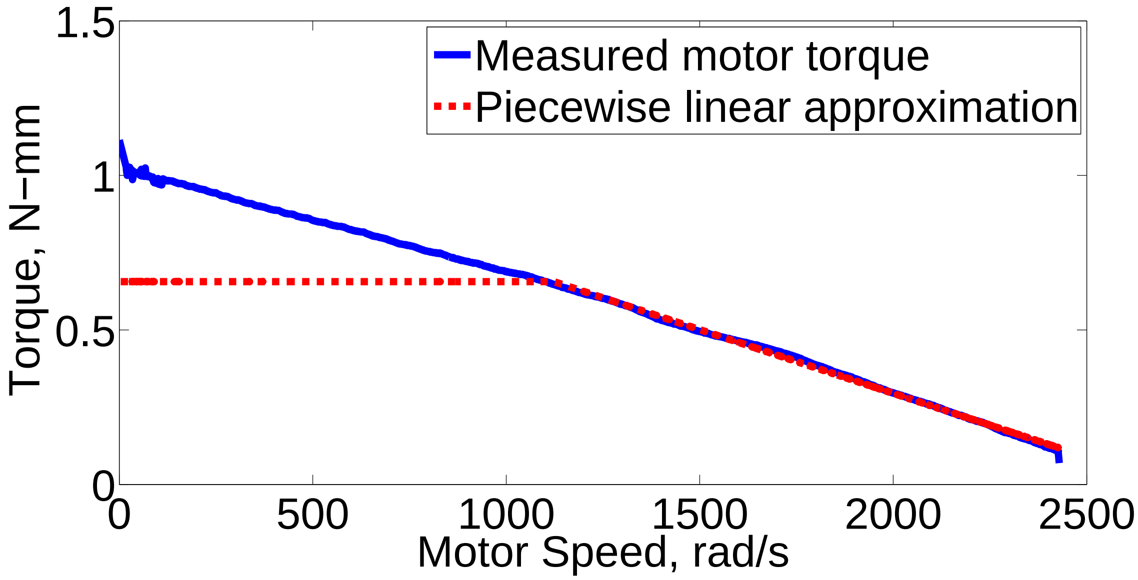

Figure 3.2: Measured motor torque compared to the approximated motor torque used in the model.

3.2.2 Motor Modeling

A Didel Superslicks 7mm brushed DC motor was used to drive the tail. Testing was performed on a dynamometer to determine motor torque as a function of motor speed. As discussed in Section 4.6, the H-bridge used to drive the motor can only provide 500 mA of current, limiting the maximum torque of the motor. For this reason, a piecewise linear torque model was employed, with a flat torque section for low speeds and a linearly decreasing section for high speeds, as shown in Figure 3.2.

The motor speed and torque can be calculated as follows

$$\omega_{mot} = \eta\dot{\psi} \tag{3.18}$$

$$T_{mot} = \frac{T}{\eta\alpha} \tag{3.19}$$

where η is the gear ratio of the tail transmission and α is the mechanical efficiency of the drivetrain.

3.2.3 Ground Interaction and Friction Moment

We use the Coulomb model to estimate the friction moment on the robot as the turn is made. We assume the friction produces a pure moment during the turn, and the friction moment is expressed as

$$M_f = -\mu_d(m_b + m_t)g \cdot r_{\text{eff}} \cdot \text{sgn}(\dot{\theta}) \tag{3.20}$$

where μ_d is the effective coefficient of friction, and r_{eff} is the effective radius of the moment. r_{eff} is defined to be half the diagonal length of the robot. The greatest tail torque occurs as soon as the tail is actuated, which overwhelms the static friction. As such, we only consider dynamic friction here. μ_d, which is a function of stride frequency, was measured experimentally by running the robot up a slope γ. If the robot was not able to advance upwards, but did not slide downwards, then the effective friction coefficient is

$$\mu_d = \arctan\gamma \tag{3.21}$$

This experiment was repeated for a range of leg frequencies between 0 and 13.3 Hz.

3.2.4 Comparing Theoretical Leg and Tail Yaw Rates

For turning with the tail, the motor torque limits the yaw rate. If more torque is available, the tail can be driven faster and correspondingly the robot will turn faster. Legged turning however, through friction and normal forces, and it is limited by these. We can determine a maximum theoretical turning limit for legs that are sliding on the ground and compare this to our tail turning method. For the best turning with the legs, we assume the legs on the outside of the turn are driving forward, while the legs on the inside of the turn are driving rearward. Eq. (3.22) shows the maximum moment that can be applied under sliding friction with the legs.

$$M_{\text{legs}} = \mu mg \cdot a \tag{3.22}$$

Applying this moment over a time interval changes the yaw rate of the body, which we can then compare to our model of tail turning as a function of dynamic coefficient of friction. The time used is 150 milliseconds, to accord with the physical experiments performed in section 3.6.2. Figure 3.3 shows the results of this comparison.

Without friction, the legs are unable to turn the robot at all, while the tail turns the robot at 530 $^\circ sec^{-1}$. At a friction coefficient of about 0.22, both methods are turning the robot at about 240 $^\circ sec^{-1}$. With a friction coefficient of 0.5, the tail can produce a yaw rate of only 10 $^\circ sec^{-1}$while the legs could theoretically produce 540 $^\circ sec^{-1}$. Legged turning in this manner would be difficult or nearly impossible while the robot is running at high speed, but this limitation does not apply to tail steering. Effects of leg compliance are not considered in this analysis.

An important consideration not addressed in Fig. 3.3 is that of duty factor. In the analysis above, a constant normal force during running is assumed. If the normal force on the robot varies over the stride, the effective coefficient of friction could be much lower than what is measured statically. If an airborne phase occurs, the friction is essentially zero, independent of the surface media. Inertial steering torque, however, can be applied by the tail actuator 100% of the time, making the results shown in Fig. 3.3 conservative with respect to inertial steering, and represent a

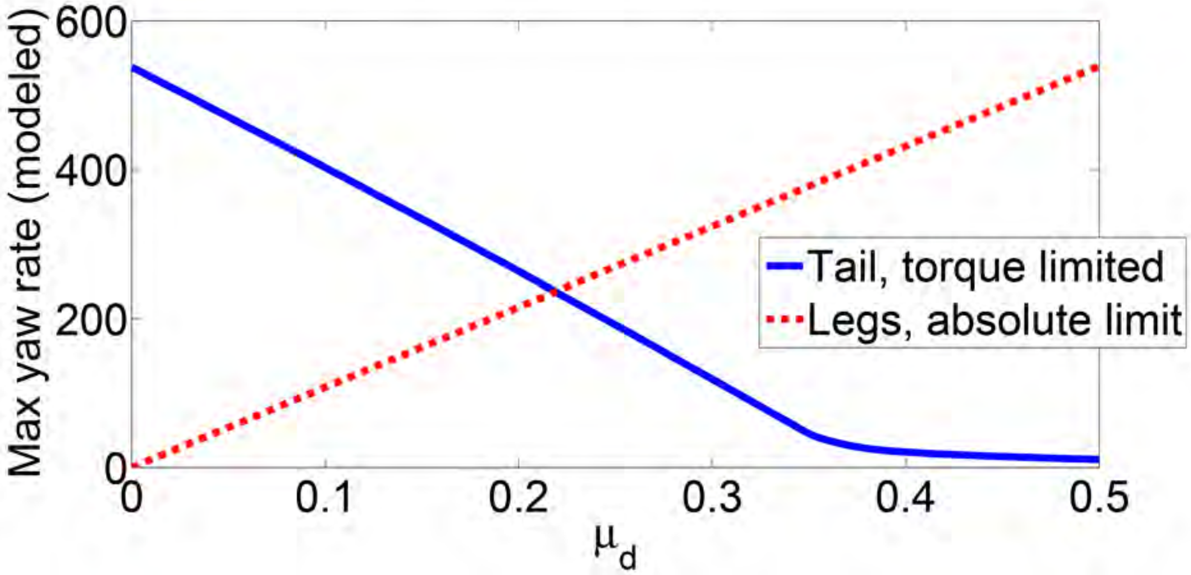

Figure 3.3: As friction increases, legged turning becomes more effective, and tail turning loses effectiveness. However, the tail steering can be applied while the robot runs without losing forward speed. This would be difficult or impossible for the legged steering. This assumes the best case for legged steering is Eq. (3.22).

best case for legged steering.

It is also important to note that the tail turning is limited by the torque of the motor. If the motor torque increased, higher turning rates would be achieved, whereas the legged results are fundamentally limited by friction. Finally, it is noted that the legged results are theoretical, and that the best published yaw rates using legs are currently 230 $^{\circ}sec^{-1}$[31].

3.3 Sensitivity and Design

We can use the model to inform the design of the tail. By examining the sensitivity of the body yaw rate to tail length and mass we can choose a tail that will allow the robot to turn quickly and perform well in small spaces for maximum maneuverability.

Figure 3.4 presents the body yaw rate as a function of tail mass. The graph is normalized such that the maximum yaw rate over all masses has a value of 1. Diminishing returns can be found from increasing tail mass. Maximum yaw rate occurs with a 7 gram tail weight, but at 4 grams, we see 96% of the performance for less than 60% of the weight.

Figure 3.5 shows how the body yaw rate varies with tail length. The graph is normalized in the same way as Figure 3.4. Again, we see diminishing returns with an increasing tail length. Here, our length choice of 10.2 cm provides 84% of the maximum potential performance while keeping

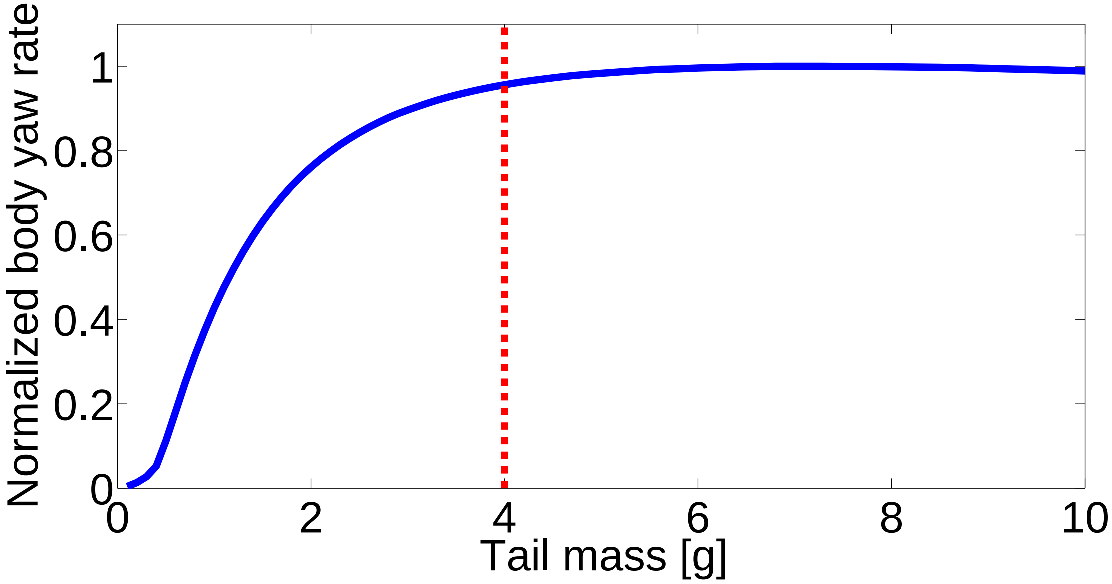

Figure 3.4: Modeled normalized body yaw rate as a function of tail mass, assuming maximum effort tail actuation.

the tail length similar to the body length. Doubling the tail length to 20.4 cm would only give a 17% relative improvement over the 10.2 cm tail, but the ability to maneuver in small spaces would be greatly compromised.

3.4 Aerodynamic Model

SailRoACH can be equipped with a sail, as discussed in Section 4.4.1. The sail is positioned at the end of the tail. While the robot runs forward with an alternating tripod gait, the sail produces drag and lift forces that cause the robot to turn. An empirical aerodynamic model was developed to help choose the best static sail position for turning. Figure 3.6 shows a representation of the robot-sail system.

3.4.1 Aerodynamic Force Modeling and Wind Tunnel Measurements

The sail can induce a moment on the robot through aerodynamic drag and lift forces. We assume that the force produced by the sail follows the equation:

$$F = (1/2)\rho C A v^2 \tag{3.23}$$

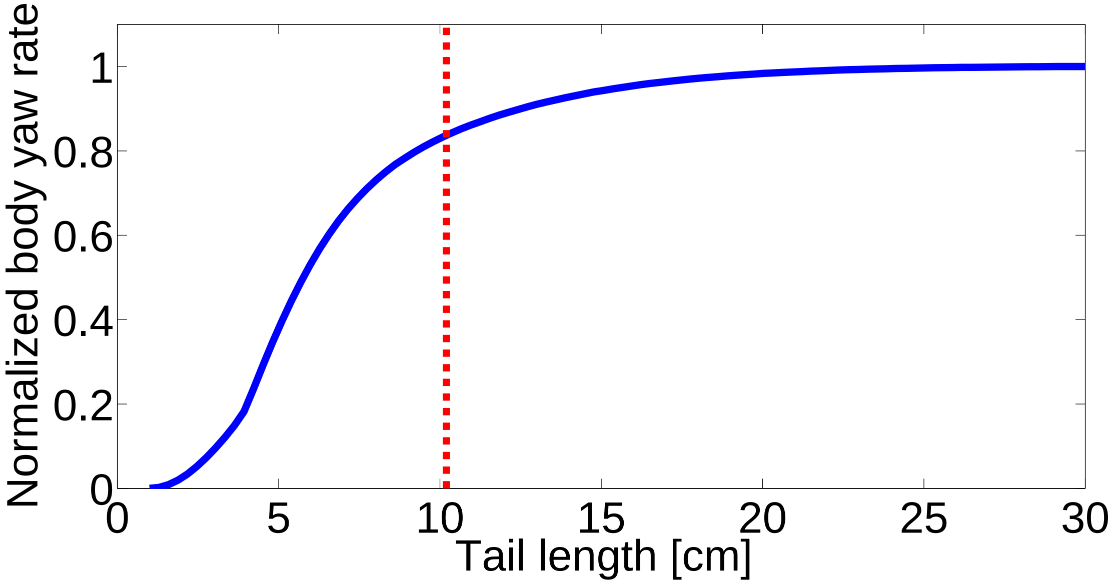

Figure 3.5: Modeled normalized body yaw rate as a function of length, assuming maximum effort tail actuation.

where ρ is the density of air, C is the non-dimensional aerodynamic coefficient, A is the surface area of the sail, v is the wind speed, and F is the force on the sail.

To test this model, and determine the aerodynamic coefficients, we gathered data in a wind tunnel (Aerovent, Inc.) with a square cross section of 0.61 m^2 using an ATI Nano-17 6-axis force transducer. The yaw moment produced by the sail on the robot is determined by the component of aerodynamic force normal to the sail (F_n).

$$T = F_n \cdot l \tag{3.24}$$

where T is the torque, and l is the distance from the sail to the center of mass of the robot.

Fig. 3.7 shows the measured force perpendicular to the sail at wind speeds from 0 to 2.25 ms^{-1} in 0.25 ms^{-1} increments and at angles of attack from 0° to 75° in 15° increments. Fig. 3.7 only shows data from 15°, 30° and 45° for clarity, as 60° and 75° were not appreciably different from the 45° measurements.

Along with the normal force on the sail, the drag force also affects the ability of the robot to turn by limiting the forward velocity, and can be calculated:

$$\begin{bmatrix} \cos(\alpha) & \sin(\alpha) \\ -\sin(\alpha) & \cos(\alpha) \end{bmatrix} \begin{bmatrix} F_t \\ F_n \end{bmatrix} = \begin{bmatrix} F_d \\ F_l \end{bmatrix} \tag{3.25}$$

where α is the sail angle, F_d is the drag force, F_l is the lift force (lateral to the robot), and F_t is the

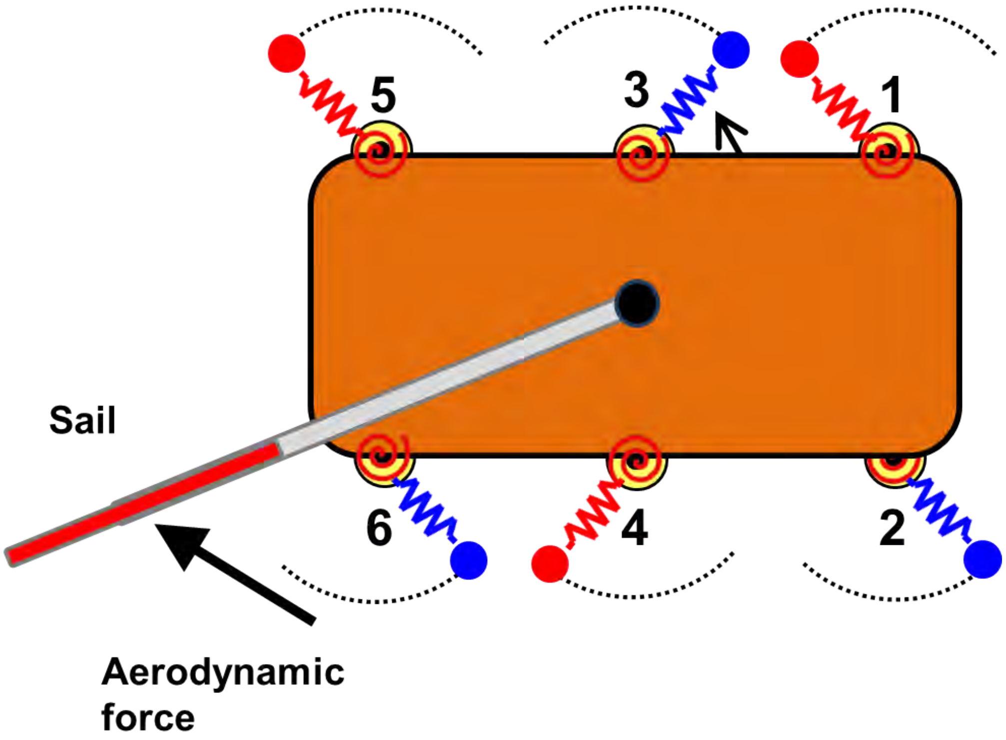

Figure 3.6: A diagram of SailRoACHrunning forward with an alternating tripod gait. The left tripod is comprised of legs 1,4,5 and the right tripod is comprised of legs 2,3,6.

force tangential to the sail.

Table 3.1 shows the yaw moment and drag coefficients across a range of sail angles based on fitting the data from our wind tunnel experiments to Eq. 3.23. For the best aerodynamic turning, the yaw moment coefficient should be maximized and the drag coefficient minimized. An angle of 30 ° shows a good operating point, and was used for experiments.

Table 3.1: Yaw moment and Drag Coefficients

Sail Angle	C_n	C_d	$\frac{C_n}{C_d}$
15 °	0.27	0.34	0.79
30 °	1.20	0.85	1.41
45 °	1.60	1.28	1.25
60 °	1.54	1.41	1.09
75 °	1.57	1.54	1.02

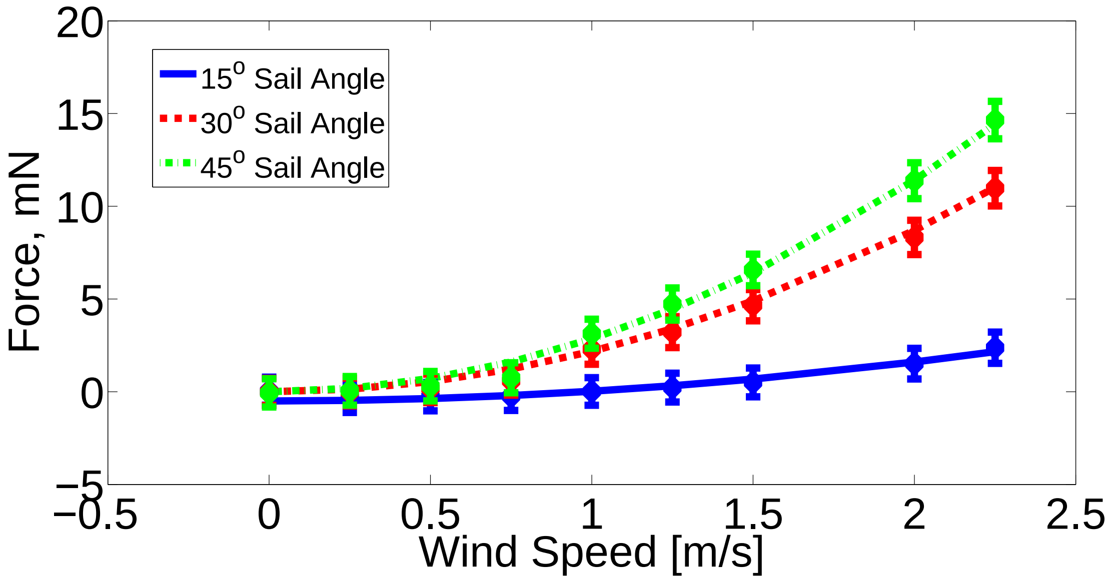

Figure 3.7: Wind tunnel results for 15 °, 30 °, and 45 ° sail angles. 60 ° and 75 ° sail angle data are omitted for clarity. The data points were obtained from the wind tunnel, shown with error bars representing ± 1 s.d. The lines represent the model from Eq. 3.23 using the values for C_n shown in Table 3.1.

3.5 Discussion of Scale Effects

Scale effects can be an important consideration. Concepts tested on Meso-scale robots may be more powerful at larger or smaller scales, or conversely, may not be applicable at all at a different scale. This analysis allows us to examine the relative effectiveness of inertial and aerodynamic tail turning at other scales. Here, the characteristic length of the robot, L, is used as the primary scaling factor.

3.5.1 Inertial Tail Turning

To examine the scale effects of inertial tail turning, Equation 3.16 is simplified by assuming the tail is mounted at the center of mass of the body ($b = 0$). Johnson et. al [18] shows that this assumption does not yield large errors for a similarly scaled robot. Walter et. al [44] discuss how rotational inertia scales for certain rodents and lizards.

$$\begin{bmatrix} I_b & 0 \\ 0 & l^2 k \end{bmatrix} \begin{bmatrix} \ddot{\theta} \\ \ddot{\phi} \end{bmatrix} = \begin{bmatrix} -T + M_f \\ T \end{bmatrix}$$

From Eq. (3.26) we determine that

$$\ddot{\theta} = \frac{-T + M_f}{I_b} \tag{3.26}$$

As shown in Hunter et. al [16], motor torque scales with L^3. However, friction on the body scales with characteristic length to the fourth power.

$$M_f = \mu mgr \sim mL \sim L^4 \tag{3.27}$$

while I_b scales with L to the fifth power.

$$I_b \sim mL^2 \sim L^5 \tag{3.28}$$

Consequently, angular acceleration is inversely scaled with characteristic length.

$$\ddot{\theta} \sim \frac{L^3 + L^4}{L^5} \sim \frac{1}{L} \tag{3.29}$$

Hence, small robots are better equipped than larger robots to take advantage of inertial turning effects.

3.5.2 Aerodynamic Tail Turning

Aerodynamic effects are greatly influenced by scale. Here, the effects of scaling on steering aerodynamics is examined, again using the characteristic length of the robot, L, as the main scaling factor. By assuming dynamically similar systems, one expects the running speed of a robot to vary with the square root of characteristic length [5].

$$v \sim L^{0.5} \tag{3.30}$$

From Eq. (3.23), we see that aerodynamic force then scales with length cubed,

$$F \sim L^2 v^2 \sim L^3 \tag{3.31}$$

while aerodynamic torque scales with length to the fourth power.

$$T \sim FL \sim L^4 \tag{3.32}$$

This means that the angular acceleration varies inversely with characteristic length.

$$\alpha = \frac{T}{I_b} \sim \frac{1}{L} \tag{3.33}$$

Thus, if there are no other torques present, a smaller robot will be turned more than a larger one. This analysis ignores effects of a changing Reynolds number, which may affect the parameter C_d in Eq. (3.23), or may make the equation invalid altogether. For scales where Equation 3.23 still holds, small robots can take advantage of aerodynamic turning better than larger robots.

Experiments (see Section 5.4) show that the angular velocity during steady state running with the sail deployed is nearly constant. This indicates that the legs must provide an equal and opposite counter-torque. The scaling of this effect is examined in [25] by Zarrouk. Zarrouk observes that previous work [47][3] shows that the speed of a robot linearly decreases as a steeper slope is ascended. This leads to the conclusion that a resistive force (on a slope gravity, on SailRoACH, aerodynamic forces) slows the robot linearly. While ascending a slope, both the right and left legs are affected by the resistive gravity force equally. However, when subjected to aerodynamic forces an torques, these resistive forces load the robot's right and left legs unequally, causing a resistive torque. Zarrouk further shows that this resistive torque causes the yaw rate during aerodynamic turning to be inversely proportional to the square root of the characteristic length, assuming Eq. 3.30 holds.

$$\dot{\theta} \sim \frac{1}{\sqrt{L}} \tag{3.34}$$

3.5.3 Skid Steering

Though this work does not focus on skid steering (analogous to a tank), the scale effects are examined here to serve as a comparison to inertial and aerodynamic turning.

Skid steering relies on the friction from the legs to produce a turn. The friction torque that the legs of a robot can produce are proportional to its mass and size.

$$T_f = \mu m g r \sim mL \sim L^4 \tag{3.35}$$

Again we see that because inertia scales inversely with characteristic length to the fifth power, smaller robots are generally more effective at differential drive steering than larger robots.

$$\alpha_{skid} = \frac{T_f}{I_b} \sim \frac{1}{L} \tag{3.36}$$

3.6 Physical Verification

3.6.1 Robot in Free Fall

To test the model without the complications of friction, the tail was actuated at maximum effort for 150 milliseconds while the robot was in free fall. This provides a zero angular momentum environment in which the robot can turn, as well as serving as a benchmark for terrestrial turning. In Figure 3.6.1 we see the results of this experiment and a comparison to the model discussed in Section 3.2.

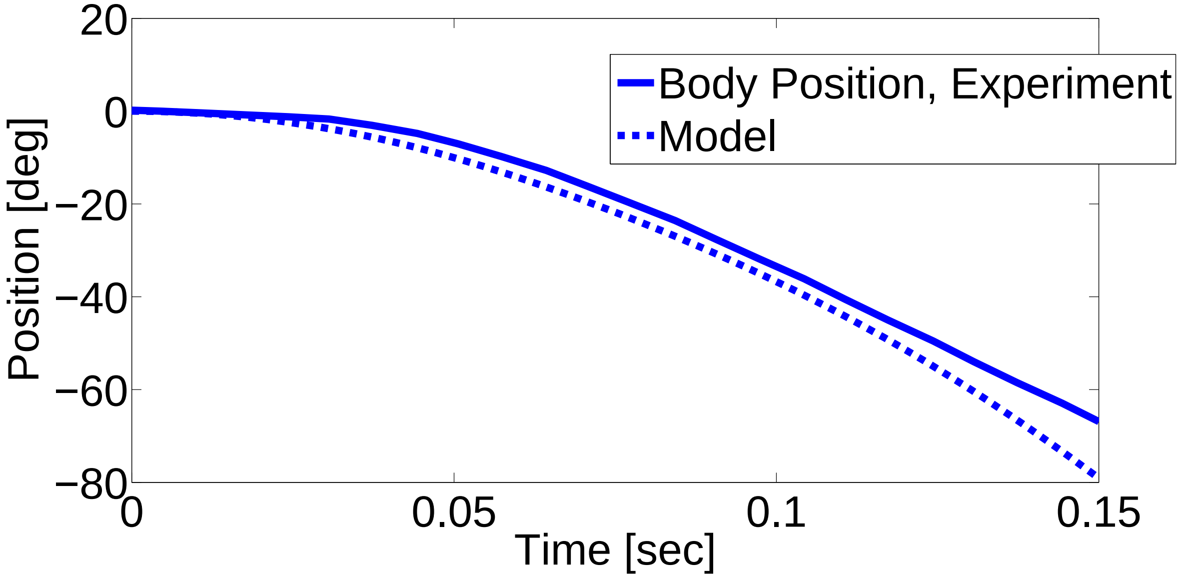

Figure 3.8: The robot turns at almost $450°sec^{-1}$in free fall. The model shows good agreement with the experiment.

The model accurately matches the results of the experiment. In the experiment, the robot turns at an average of 447 $°sec^{-1}$, compared to 530 $°sec^{-1}$for the model. Much of the difference may be due to the fact that the motor does not start developing torque exactly at zero seconds in the experiment. If we assume a lag of 50 milliseconds, there is almost no discrepancy. The turning rate of 530 $°sec^{-1}$represents an upper bound on performance with respect to our model, although unmodeled effects while the robot is on the ground, such as leg compliance, could increase the turning rate beyond this limit.

3.6.2 Effect of Running Speed on Tail Efficacy with Open Loop Actuation

For agile locomotion, it may be desirable to run the robot at a range of speeds. Experiments were performed to determine how the performance of the tail system varied with running frequency. If the variance were low, open loop control with the tail could be possible. Additionally, these tests would reveal the maximum change in body angle that could be produced by the tail at various leg frequencies. Experiments consisted of the robot running straight for one second with leg steering control [37] activated, then simultaneously turning off the leg steering control and actuating the tail at maximum effort. The tail actuation induces a turn in the robot, which is measured with the MEMS gyroscope. The experiment was done over irregular floor tile, at 8 different leg frequencies between 0 and 13.3 Hz. At each leg frequency considered, 10 trials were performed for a total of 80 experiments. Leg frequencies between 0 and 3 Hz are not well controlled and were not tested.

Figure 3.9 shows the results of these experiments. As leg frequency increases, the effective coefficient of friction generally decreases and then levels off at high frequencies, as shown in [37]. This produces a higher body yaw rate at higher leg frequencies, from 296°sec^{-1}at standstill to 344°sec^{-1}at 3.3 Hz to 401°sec^{-1}at 10 Hz. A possible explanation for the decrease and leveling off of the coefficient of friction is that at low frequencies, the legs are sticking and slipping, yielding a coefficient of friction somewhere between that of static and dynamic. At higher frequencies slip dominates and only dynamic friction is observed. A Student's t-test reveals statistically significant differences ($p<.05$) between 3.3 Hz, 6.7 Hz, and 8.3 Hz, while the turning rates at higher frequencies are not statistically significantly different from each other.

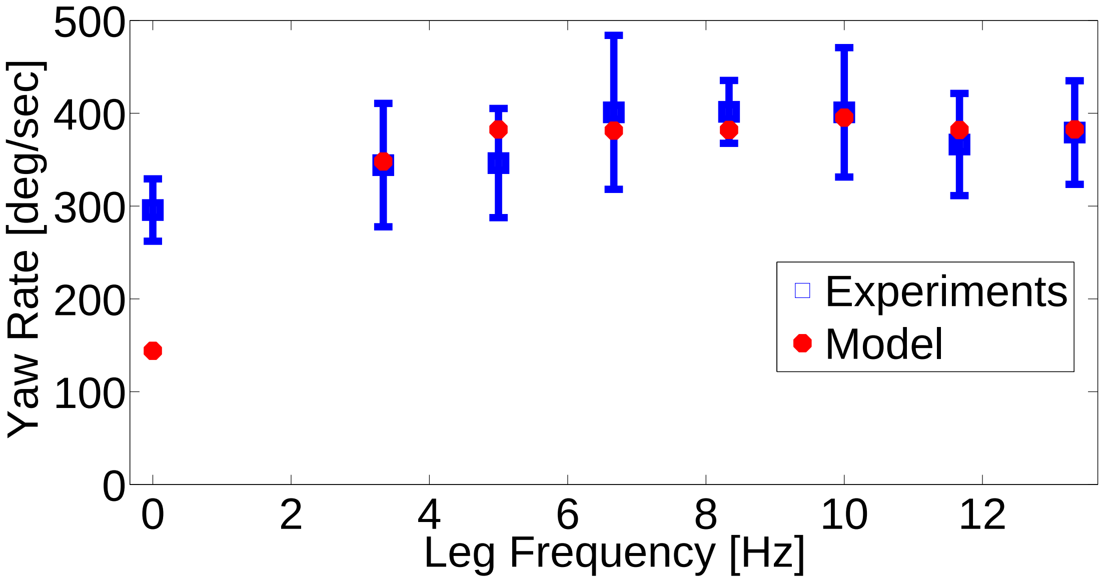

Figure 3.9: Results from open loop trials on tile surface. The square markers indicate the mean yaw rate of the robot body during the experiments, while the bars show plus or minus one standard deviation away from this mean. The circles show results from the model detailed in section 3.2. As leg frequency increases, turning performance increases and then levels out.

As shown in Figure 3.9, the model matches the experiments well for trials where the robot is running forward. At 10 Hz leg frequency, the error is 1.5%. At 5 Hz the model performs the worst, with an error of 13.4%. The total average error is 3.5%. For trials at 0 Hz, the model does not match the experiment well, with an error of -50%. The robot body is able to shift without the legs moving, as the hip flexures act as springs. This may explain the discrepancy, and a more appropriate model may be a rigid body rotating in the horizontal plane on a torsional spring.

It is also interesting to note places where the experiment slightly outperforms the model - most models are idealizations and show better than real-world performance. For this work the stochastic nature of the leg contact means that the friction used in the model could be overestimated. For example, if the robot's airborne phase is significant during the tail flick, this may lead to lower overall friction, since the full weight of the robot and tail is not on the legs at all times. This variation shows that consistent turning cannot be done open loop, and feedback control is necessary.

Chapter 4

Mechanical Design, Software, and Evolution of the Tail

Several versions of the tail mechanism were developed over time and used in various experiments. Initial tail development focused on off the shelf solutions to provide a "proof of concept," showing that a tail could be used to generate a terrestrial turn. These solutions were not found to be suitable for high performance, and so custom tail hardware and software was created. This chapter briefly covers initial tail development, then details the design and capabilities of the three tails used to perform experiments featured in this work.

4.1 Initial Tail Development

In initial development, off-the-shelf servomotors were used to drive the tail. These are easy to obtain, and come with control built in, but suffer several disadvantages. Servos are generally built for high-torque, low-speed applications, though high-speed is necessary here. This was addressed by physically opening the servo housing, removing a gear, and fusing two gears together by soldering iron (plastic weld) or glue. This produced higher tail speeds, but meant low available torque, and less accurate built-in control. Modification also reduced the off-the-shelf advantage. Additionally, servos are heavy (about 8 grams), and do not integrate well into our robot platforms.

The tail itself was constructed of a cardboard SCM adapter holding a carbon fiber rod to the servo, and another cardboard SCM piece with embedded magnets to allow for adjustable ballast.

This tail was useful for executing early experiments of tail turning. The robot, OctoRoACH+Tail, has peak yaw rates of 400°sec^{-1}at 4 Hz actuation frequency, but cannot produce sustained turns at this rate. Detailed results can be found in [37]. OctoRoACH+Tail can be seen in Fig. 4.1.

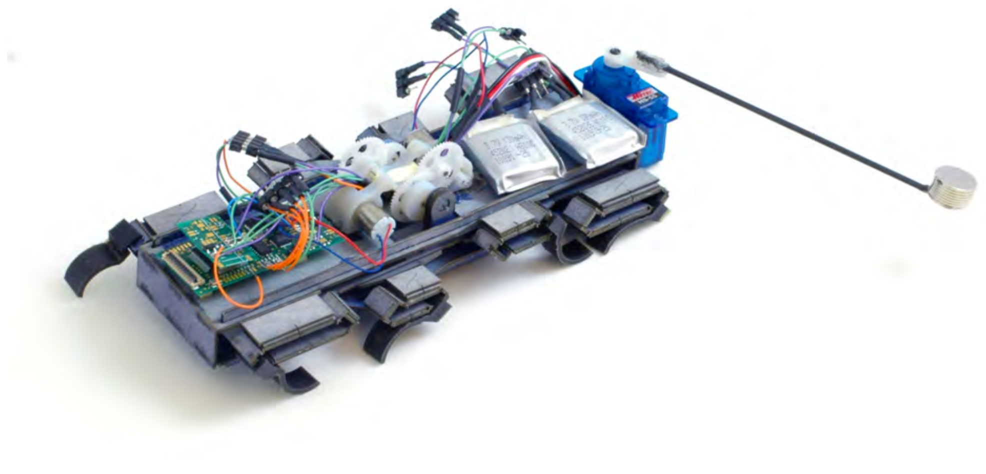

Figure 4.1: The OctoRoACH+Tail. This early tail prototype used modified off the shelf parts.

4.2 Torque Controlled Tail

From the initial experiments, it became clear that a higher powered tail was necessary. Furthermore, the control of the servomotor was limiting, as only the position could be chosen, but not the delivered torque. To solve these problems, Tail Design I (TD I) was developed. An isometric view of TD I is shown in Fig. 4.2. A top view can be seen in Fig. 4.3.

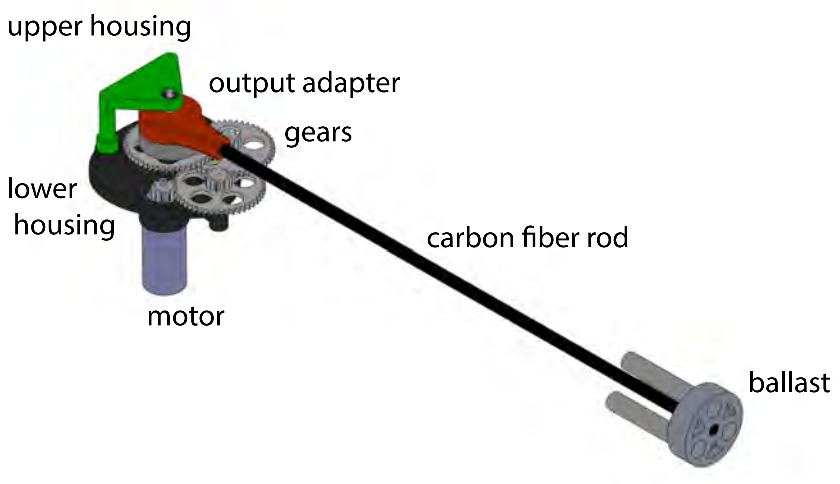

Figure 4.2: Isometric view of Tail Design 1. The tail does not have sensors, and must be torque controlled.

The components of the tail mechanism include the DC motor, a pinion gear, three spur gears, a custom adapter to join the tail rod and the gears, a custom two piece transmission housing that holds the motor and gears in place and provides bearing support, a carbon fiber rod to serve as the length of the tail, and a custom printed ballast piece, fitted with steel dowel pins to provide weight. A 1 mm ID ball bearing allows free movement of the tail with respect to the bearing support. The tail is 11.5 cm long, and the ballast on the end weighs 4 grams.

The tail has a gear ratio of 85.3:1, chosen because high torque was necessary to cause the legs of the robot to leave the static friction regime when actuating the tail. It was also chosen because it could be built with off-the-shelf gears.

The tail has no sensors, so the only control available is torque control. This limits the variety

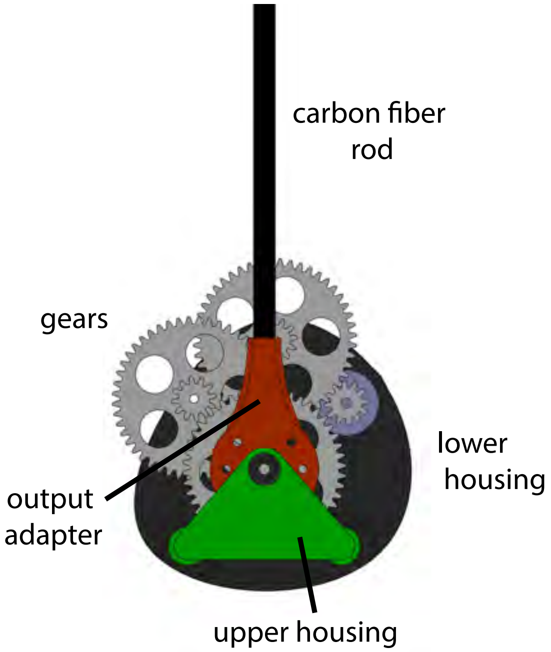

Figure 4.3: Top view of TD 1. The 7 mm DC motor drives the tail through an 85.3:1 gear ratio.

of experiments that can be performed, but is suitable for open loop tests of turning ability. The bearing support piece limits the range of motion of the tail to 260 degrees. If the end of the range of motion is reached, the tail collides with the bearing support, stopping the tail abruptly and creating an impulse moment detrimental to the robot's turning performance. However, due to the lack of feedback, the physical stops are useful for experiments. The tail can be positioned while the robot is not moving by applying a small amount of torque over time, ensuring the tail rests on a stop. At this point the robot can be given commands (such as running forward) and the tail can be actuated with the full range of motion available.

Tail Design I was fitted to TAYLRoACH I (Tail Actuated Yaw Locomotion Robotic Autonomous Crawling Hexapod), whose chassis is adapted from the VelociRoACH design [10]. TAYLRoACH I is shown in Fig. 4.4.

TAYLRoACH I is a 45 gram hexapedal robot that features three 7 mm brushed DC motors, two of which independently control a set of 3 legs on either side of the robot. This allows the robot to steer using its legs alone as detailed in [37], while the final motor drives the tail. The tail mechanism is shown in greater detail in Fig. 4.5. As discussed in Section 5.1, TAYLRoACH I is capable of 90 degree turns at $400^\circ sec^{-1}$.

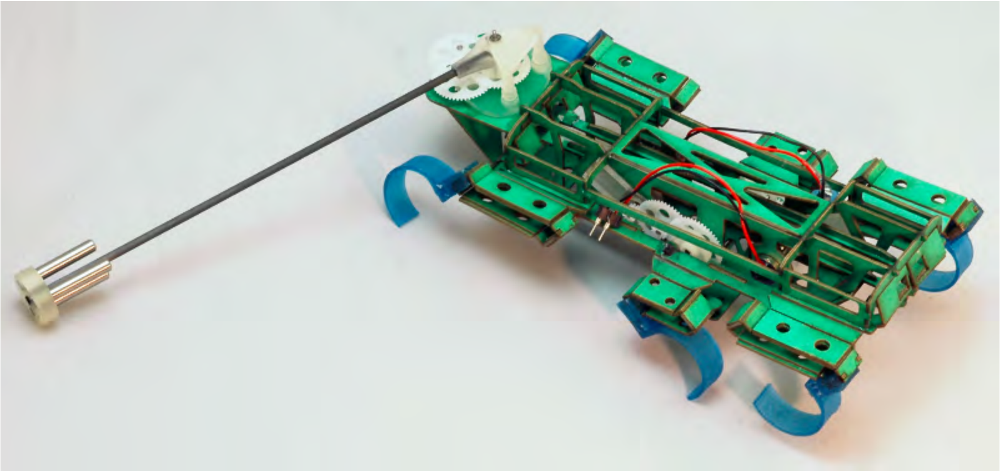

Figure 4.4: TAYLRoACH I, used for determining open-loop body yaw response.

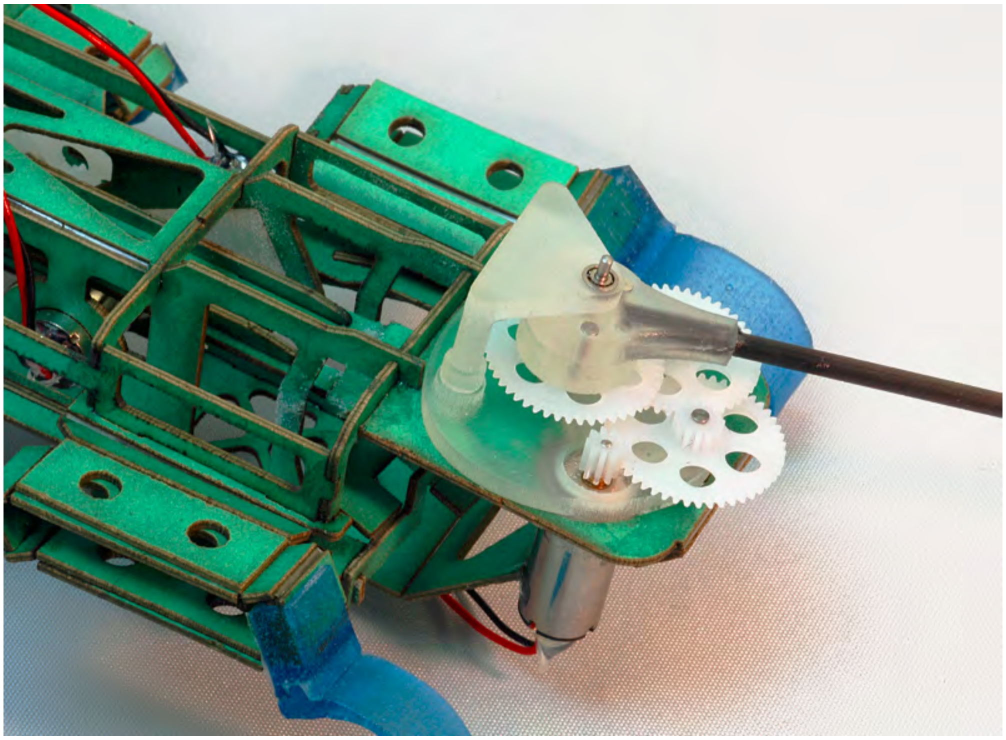

Figure 4.5: Close up view of tail mechanism.

4.3 Tail with Position Feedback

Tail Design II (TD II) features position feedback for the tail, and design improvements that allow for better performance. These improvements include a more compact design, less parts and a revised gear ratio. Due to their size, packaging considerations are critical on a millirobot. To this end, a worm gear was used in place of a pinion gear, greatly improving packaging, as discussed in Section 4.3.1. An isometric view of TD II can be seen in Fig. 4.6. A top view of TD II can be seen in Fig. 4.7.

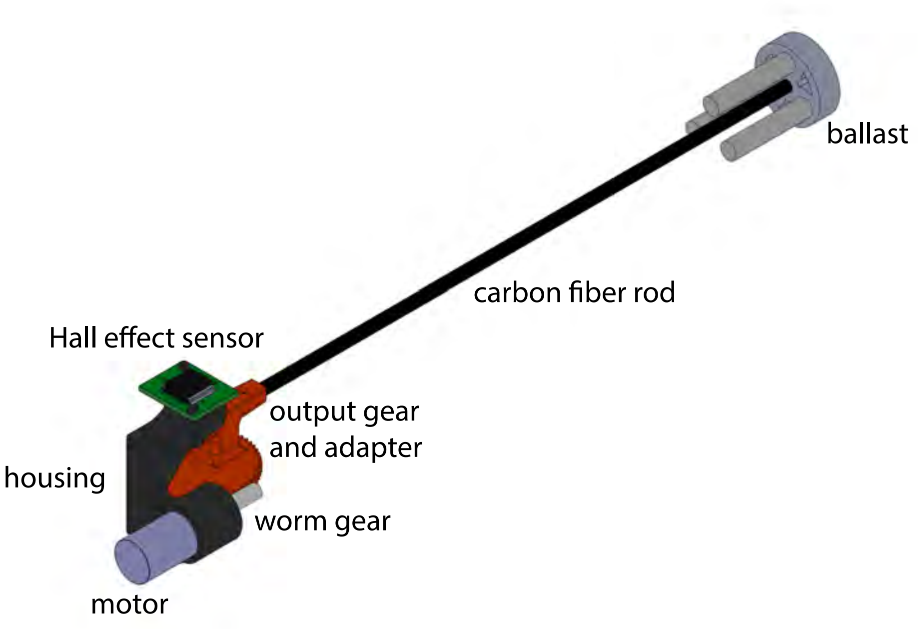

Figure 4.6: Isometric view of Tail Design II. The diametrically polarized magnet used for the Hall effect encoder and the ball bearing are not shown.

4.3.1 Worm Gear Drive

One of the largest differences between TD I and II is the use of a worm gear to drive the tail. Using a worm gear has several advantages for this application, especially for packaging. In this case, the worm gear allows the motor axis to be oriented in the horizontal plane. In the TAYLRoACHchassis, there are many moving parts just below the top of the chassis. In TAYLRoACH I the motor and tail transmission must be mounted behind the entire leg drivetrain, to not interfere with its moving parts. The use of the worm gear allows the tail to be mounted on top of the main chassis, closer to the robot's center of mass. This reduces the moment of inertia of the robot significantly, as the tail is a heavy component at the very end of the body. This difference is shown in Fig. 4.8, and in Fig. 4.9.

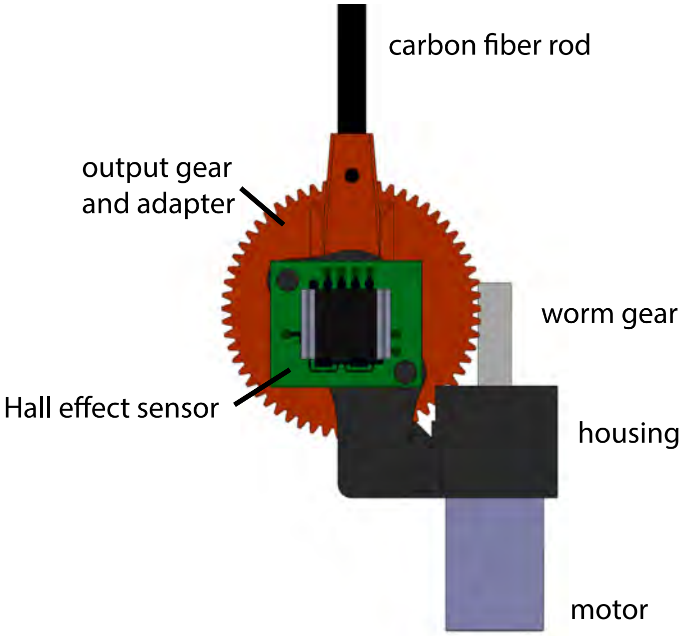

Figure 4.7: Top view of TD II. The TD II transmission features only a single gear that, coupled with the worm gear on the motor, gives a 60:1 gear ratio.

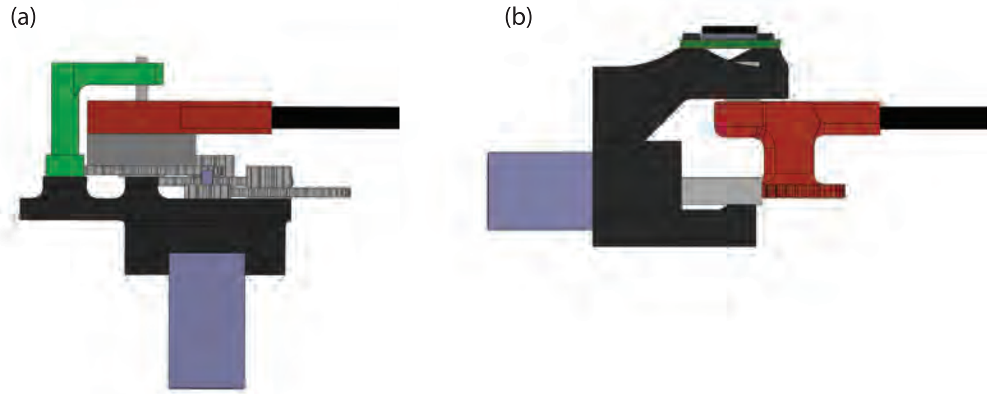

Figure 4.8: (a) TD I uses spur gears, necessitating a large vertical footprint. (b) TD II employs a worm gear, making for a more compact design.

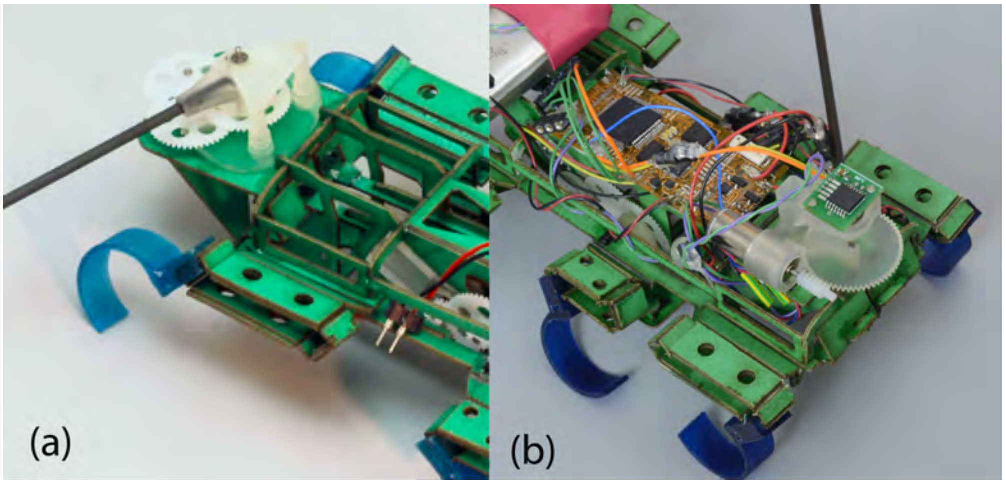

Figure 4.9: (a) TAYLRoACH I must mount the tail behind the rear hips, to prevent colliding with the leg drivetrain. (b) TAYLRoACH II has its tail mounted in front of the rear hips. This brings the tail closer to the center of mass of the robot, reducing yaw moment of inertia.

TAYLRoACH II uses a 60:1 gear ratio. This requires one gear instead of the three used on TAYLRoACH I. Considering the reduction of accompanying pins, this causes the part count to go down significantly.

A disadvantage of the worm gear is its dynamic behavior. High friction occurs in a worm gear, and the tail cannot be back-driven. This may be advantageous if the tail is to be kept at a static position, but usually is not useful. The lack of back-drive can make the tail difficult to work with and requires a special tool to turn easily without using computer control. Additionally, the worm gear has low efficiency (measured at 27%) and backlash of two to three degrees, due to axial displacement of the motor output shaft.

4.3.2 Transmission

The transmission housing for TAYLRoACH II is a single piece, and allows a range of motion of 300 degrees. The housing holds the motor, the output gear, and provides bearing support. The output gear is a 3D printed single piece which also holds the tail rod. This is stronger than TD I and uses less parts. Bearing support is provided by a 3 mm diametrically polarized magnet mounted in a 3 mm ID ball bearing, serving dual use as a magnet for the sensor and as a shaft. A section view can be seen in Fig. 4.10.

4.3.3 Position Sensor

To provide position feedback, an absolute position sensor using Hall Effect is employed. The chip is an AMS AS5048B Rotary Position Sensor. The 14 bit sensor is accurate to 0.05 degrees after

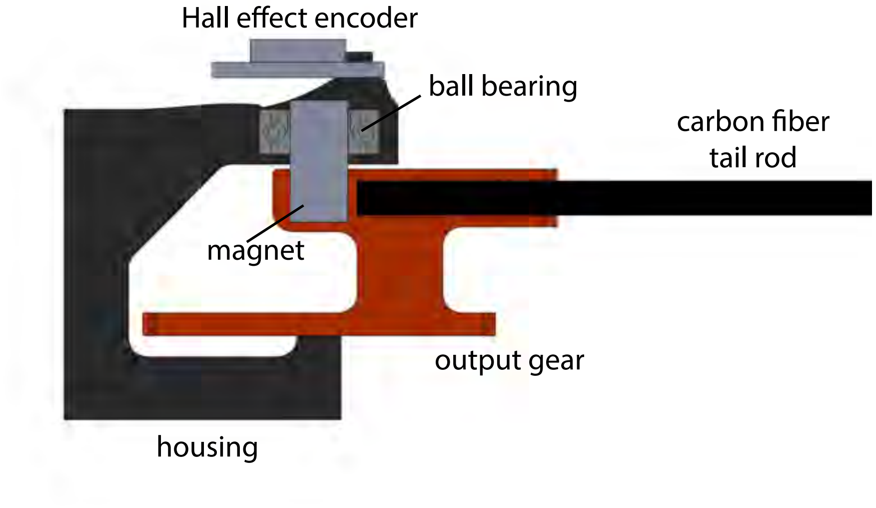

Figure 4.10: The Hall effect sensor provides position feedback for the tail.

linearization and averaging. The sensor is located by two small bosses on the transmission housing which allow for precise placement. The diametrically polarized magnet used for bearing support is mounted directly beneath the sensor. The magnet moves with the tail, while the sensor is grounded. This relative movement allows the sensor to determine the relative position between the body and the tail. The gyroscope on the robot CPU, with forward Euler integration, can measure the robot's yaw position. The combination of these two readings gives a global yaw position of the tail.

4.3.4 TAYLRoACH II

TD II was integrated into the chassis TAYLRoACH II (seen in Fig. 4.11). A closer view of the tail mechanism can be seen in Fig. 4.12. As discussed in Section 5.2.1, TAYLRoACH II is capable of 90 degree turns at $360°sec^{-1}$precise to 13 degrees and 30 or 60 degree turns at a similar yaw rate precise to less than 5 degrees.

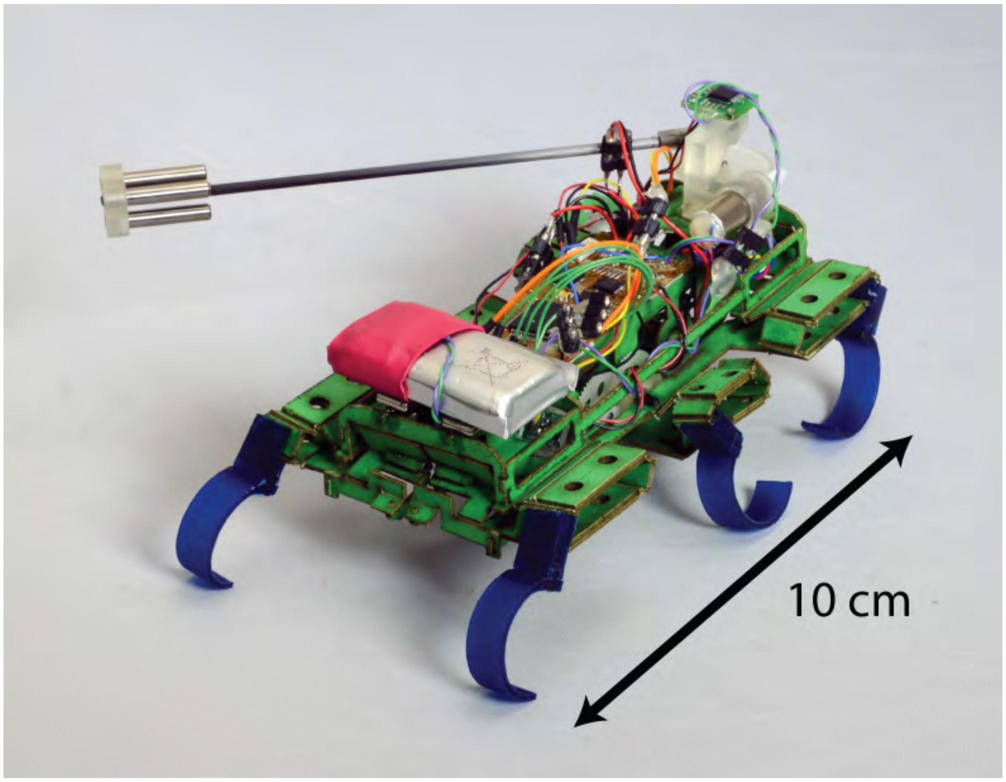

Figure 4.11: TAYLRoACH II, equipped with worm gear drive and Hall effect position sensor.

4.4 Tail with Unlimited Rotation

Tail Design III allows unlimited rotation of the tail, and for interchangeable ballast. An isometric view of the tail is shown in Fig. 4.13. A top view of the tail is shown in Fig. 4.14.

4.4.1 Modular ballast

Modular ballast allows the tail to be configured with different end pieces quickly and easily. This functionality facilitates a wide range of experiments, and expands the potential of the tail. Instead of using a weight on the end of the tail, a camera or other sensors could be added, aerodynamic elements could be used, or other modifications could be made. Modular ballast is also useful for testing hypotheses, the experiment and control case can be easily interchanged.

A single 3D printed piece attaches permanently to the tail. A second 3D printed piece holds the ballast piece. A slip fit between the two pieces allows them to mate. Two 0.75 mm pins secure the ballast to the tail, but can easily be removed, allowing the ballast to be swapped. A closeup of the ballasts can be seen in Fig. 4.15

The sail, used for aerodynamic turning, is constructed of cardboard and PET using the SCM

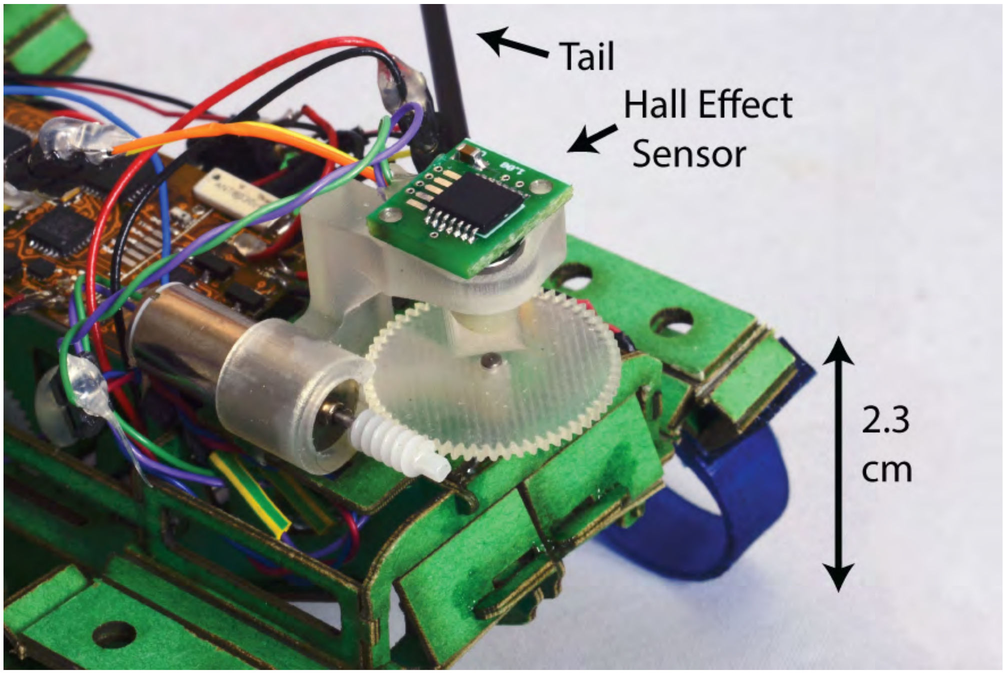

Figure 4.12: The Hall effect sensor provides position feedback for the tail.

fabrication process. It forms a 50 mm x 50 mm flat plate and weighs 0.7 grams. The carrier pieces that attach to the sail weigh a combined 2.7 grams. The "weight attachment" serves as a control case for the sail, as it has the same mass but produces little drag or lift at the running speed of the robot.

4.4.2 Unlimited Rotation Transmission

Unlimited rotation offers many advantages. The tail does not need to be "reset" after a maneuver, as all positions are roughly equivalent. To this end, the tail is now mounted in the center of the robot instead of the rear. This also reduces the moment of inertia of the robot significantly, increasing the tails effectiveness.

Bearing support is necessary for the tail to function properly, but here the support is mounted below the tail rod to avoid limiting its range of motion. The transmission housing for SailRoACH is composed of two main pieces. The lower piece holds the motor, the Hall effect sensor, and a ball bearing. The top piece press fits into the lower piece, and also holds a ball bearing. The output gear sits between the upper and lower housing. It also has a diametrically polarized magnet press fit into it, used for position sensing. The order of assembly of the transmission is important. First, the magnet of the output gear is placed into the ball bearing of the lower housing. Then, the upper housing is press fit into the lower housing, and the output gear slots into the upper housing's bearing. This provides double bearing support for the tail, making it extremely stable. Finally, a

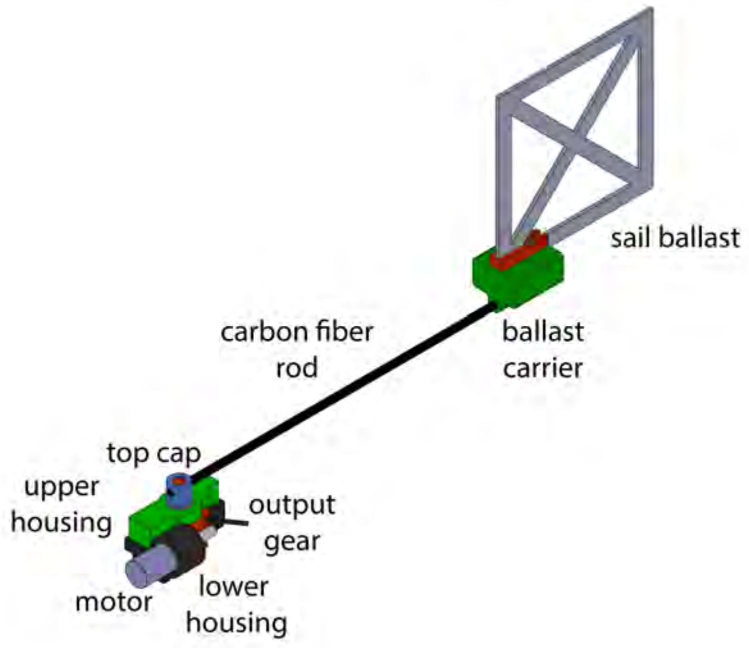

Figure 4.13: An isometric view of Tail Design III. Bearing support is now below the tail, allowing for unlimited rotation. The ballast is equipped with a sail to test aerodynamic effects.

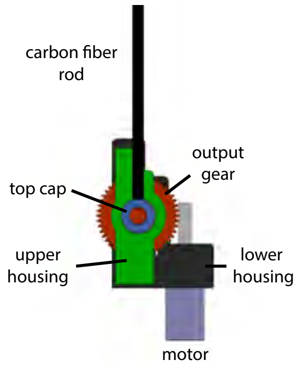

Figure 4.14: A top view of TD III. A single 48:1 output gear is driven by a worm gear.

3D printed cap goes over the top of the output gear, and the tail rod is slotted through the output gear and cap. The cap and output gear are glued together. This locates the output gear and provides a thrust constraint. The output gear is located such that it rotates while touching the moving ball bearing itself, meaning there is very little friction in the system. The cap shares shear load with the

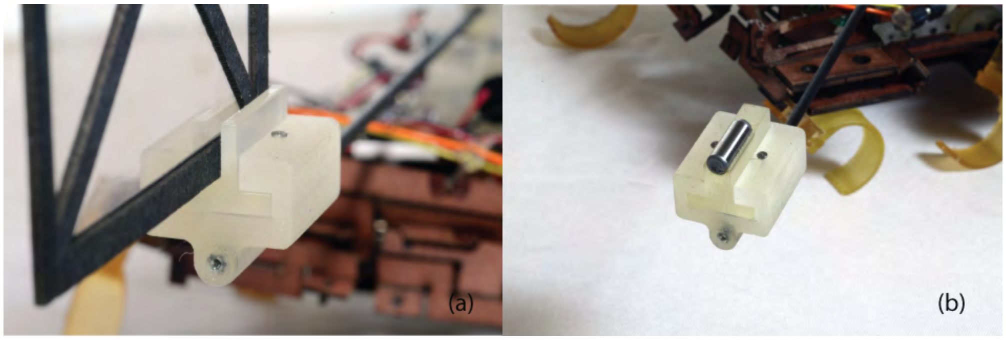

Figure 4.15: A permanent carrier piece is permanently fixed to the tail with adhesive. A second piece slip fits into the carrier piece, and holds the ballast. (a) Sail attachment (b) weight attachment

output gear, making it more robust. A section view and an exploded view are shown in Fig. 4.16.

SailRoACHis shown in Fig. 4.17, featuring different ballasts for different tasks. Tail Design III is shown in Fig. 4.18.

4.5 Powertrain Design

Choosing the correct gear ratio for the tail powertrain is important. A gear ratio that is too high will limit the maximum speed of the tail, limiting the maximum change in angular momentum. However, a gear ratio that is too low will not provide enough torque to overcome the static friction of the ground. For early designs, high gear ratios were used to ensure static friction could be overcome, but experiments revealed that the tail was speed-limited. For Tail Design III, the simulation detailed in Section 3.2 was used to determine the best possible gear ratio.

The maximum torque the motor can produce is limited by the amount of current through the motor, the motor constant, the gear ratio, and the efficiency of the drivetrain, as shown in Eq. 4.1.

$$T_{max} = k_t i_{max} \eta \epsilon \tag{4.1}$$

where k_t is the motor constant, i_{max} is the maximum current, η is the gear ratio, and ϵ is the efficiency of the drivetrain. To determine the drivetrain efficiency, the tail was rigidly mounted to a ground, and actuated at 100% effort. The tail speed and position were recorded. The tail motion should follow the equation

$$\ddot{\phi} = \frac{T_{tail}}{m_t l} \tag{4.2}$$

where $\ddot{\phi}$ is the angular acceleration of the tail, T_{tail} is the delivered torque, m_t is the tail mass, and l is the tail's length. Further,

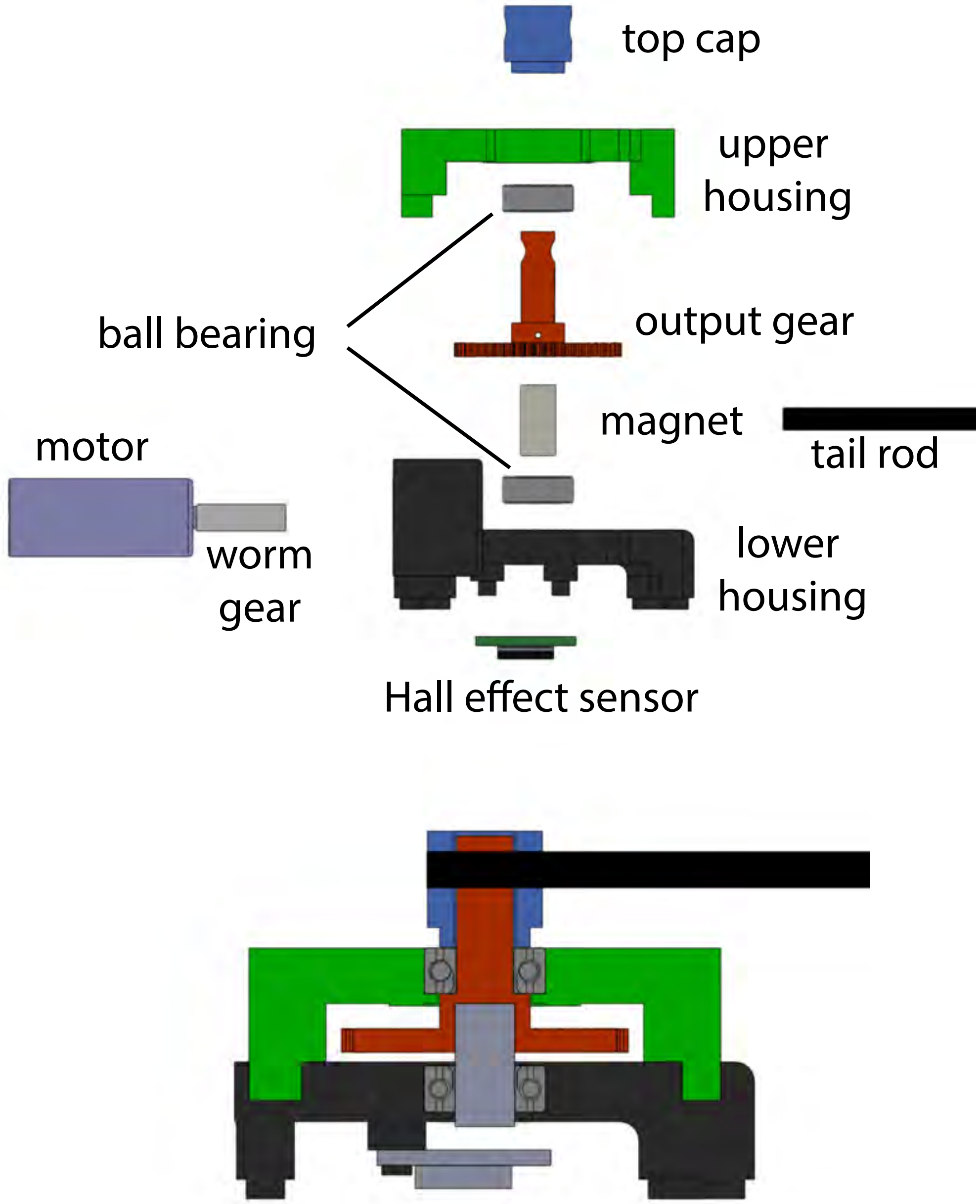

Figure 4.16: A section and exploded view of the unlimited rotation tail.

$$T_{tail} = T_{mot}\eta\epsilon \tag{4.3}$$

where T_{mot} is determined using the piecewise linear model discussed in Section 3.2.2. Using ϵ as a fitting parameter, the best fit between the experimental data and Eq. 4.3 is made. The chosen

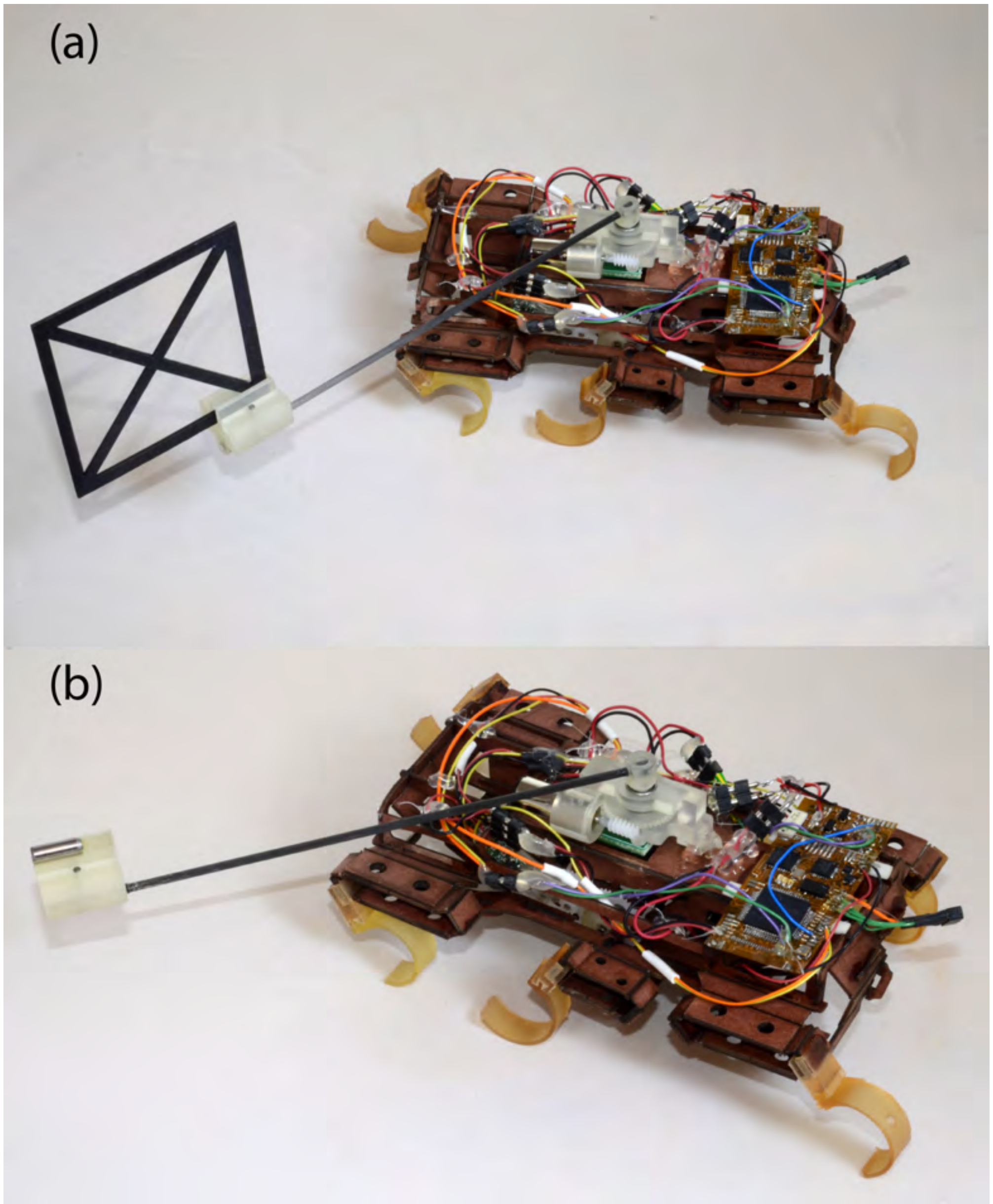

Figure 4.17: SailRoACH can be equipped with ballast of any kind, carrying aerodynamic elements, sensors, or simply weight. (a) SailRoACH equipped with the sail attachment, which generates aerodynamic drag when the tail is actuated or when the robot runs at high speeds. (b) SailRoACH equipped with a three gram weighted ballast.

ϵ is then used in the full robot system model in Section 3.2.

To determine the best gear ratio, four possible gear ratios are examined, 24:1, 36:1, 48:1, and 60:1. Multiples of 12 were used because these could be fabricated using available gear generation

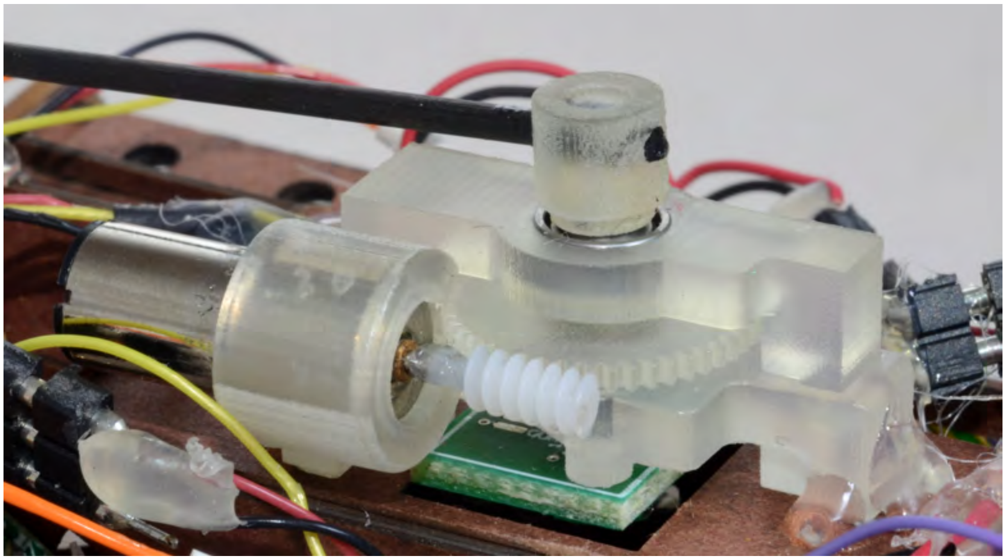

Figure 4.18: A closeup view of the Tail Design III mechanism.

software. Ratios above 60:1 were not used because experimental evidence already showed that the tail was speed limited with a 60:1 gear ratio. In simulation, a powertrain of a given gear ratio was actuated until the robot body turned 180 degrees, the maximum desirable turn. The gear ratio which was able to turn the robot 180 degrees in the least amount of time was chosen.

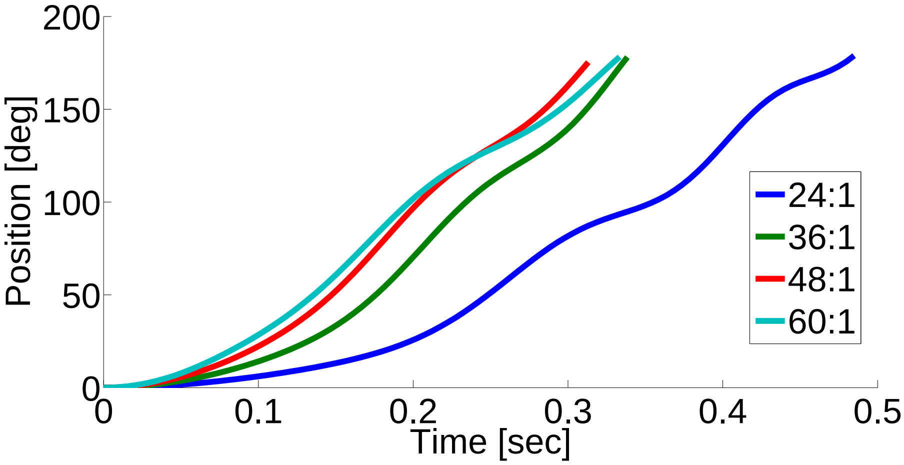

Figure 4.19: Robot body position versus time for a maximum effort actuation for different gear ratios.

As shown in Fig. 4.19, the 48:1 gear ratio performs best, turning the body 180 degrees in 0.31 seconds. 60:1 and 36:1 each take slightly longer, while 24:1 takes significantly longer at 0.48

seconds. The simulated surface is tile, where most of the inertial tail turning experiments (see Chap. 5) were performed.

4.6 Power, Communication, and Control Hardware

The robot is equipped with a control board similar to that used in [23]. A component block diagram is presented in Figure 4.20. A dsPIC33F microcontroller coordinates all the control loops, motion timing, and communication functions of the robot. The board also hosts a 3-axis MEMS chip gyroscope, and three motor drivers. Drive for the leg-actuating motors is identical to the method in [37], where each of the two legs motors are driven by a single MOFSET, providing one-direction control with no braking. Leg motor speed is sensed via back-EMF, and average motor speed is controlled via pulse-width modulation (PWM) and a PID control loop. The drive for the tail motor is provided by an integrated chip H-bridge with a current limit of 0.5 A, resulting in limited motor torque, as discussed in Section 3.2.2. The H-bridge is configured for no motor braking or current recirculation.

The magnetic position encoder for the tail described in Section 4.3.3 is connected to the CPU board via the I2C bus. Real-time telemetry is recorded onboard to a flash memory at 150 Hz and downloaded via an 802.15.4 radio after each experiment, providing a complete trace of the instantaneous inputs and outputs of each software control block, yaw rates, tail position, and motor back-EMF. After queues of motion commands are sent from a host PC system, the robot runs fully autonomously with no external control loop closure, all sensing done on-board, and millisecond accurate coordination of actuators and control goals.

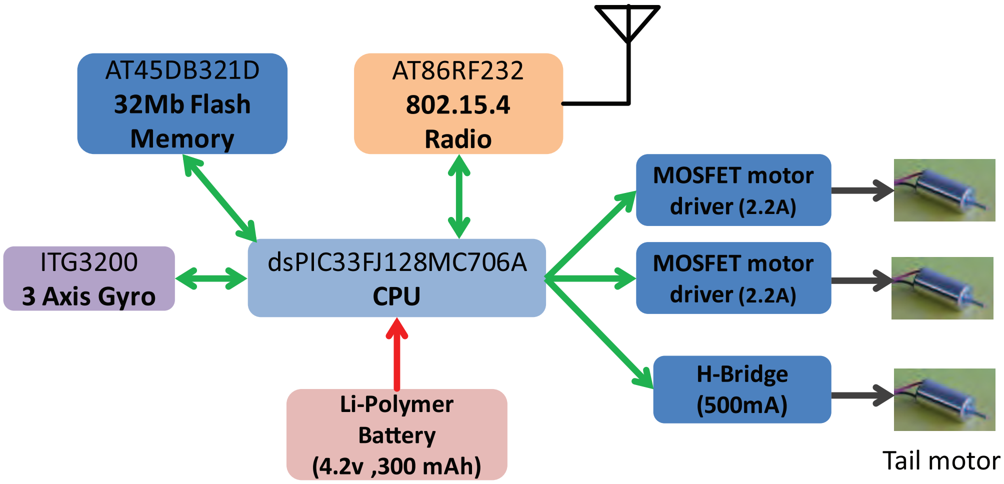

Figure 4.20: Block diagram of controller board.

4.7 Tail Software

Two feedback control policies were employed on TAYLRoACH II and SailRoACH. A PID algorithm controls the relative position of the tail and body, while a min-max or "bang-bang" controller is used to control the yaw of the robot body with the tail. These are not executed simultaneously. The relative position control is a standard PID control loop, seen in Fig. 4.21.

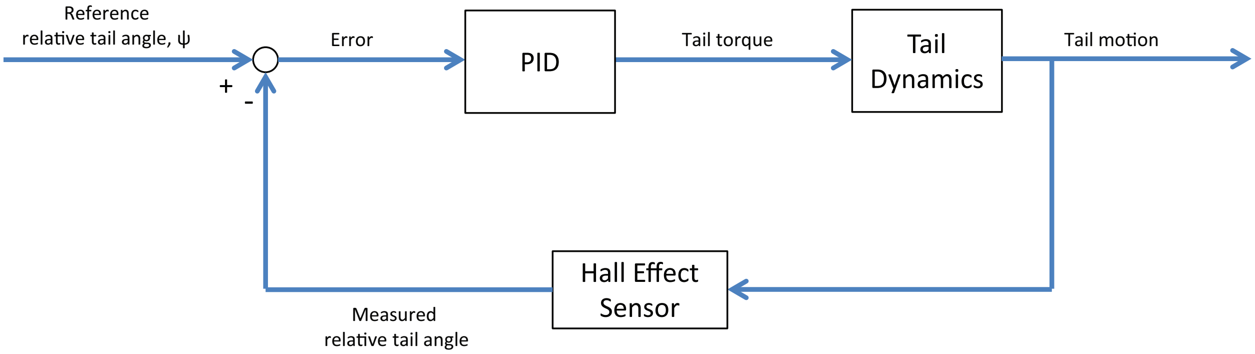

Figure 4.21: A standard PID control loop used to regulate the position of the tail relative to the body.

To control robot body position, bang-bang control is used, as detailed in Chapter 5.

Chapter 5

Experimental Results

This chapter details experimental results of inertial and aerodynamic steering of TAYLRoACH I, TAYLRoACH II, and SailRoACH. The first section details open loop actuation of the tail for inertial turning, and shows that highly rapid turns are possible, but lead to inconsistent results. The second section examines the addition of a feedback controller, and demonstrates that precision can be improved greatly with a nonlinear control strategy.

The third section of the chapter more thoroughly characterizes the performance of the inertial turning and control, while the fourth section details the consequences of the aerodynamic sail and compares those results to a non-aerodynamic control. The final section of the chapter compares inertial and aerodynamic steering to other methods of steering currently employed on legged robots.

5.1 Open Loop Actuation

TAYLRoACH I was driven from a stop on a tile surface at a fixed throttle for the legs for two seconds. The tail is initially set to its full right position, and is free, with no torque applied to it. Velocity control is implemented on the leg speeds, but neither position control of the legs nor steering control of the body is used. This means that the phasing of the left and right legs is not controlled, and there is no feedback on the robot heading to ensure straight ahead motion. One second into the experiment, the tail is actuated with maximum torque for 300 milliseconds, moving the tail from full right to full left position. Yaw data for the tail and body were recorded using an OptiTrack [1] motion capture system.

As seen in Fig. 5.1, the robot drifts before tail actuation, has a high yaw rate during the tail actuation, and then changes direction after the tail actuation, possibly due to an internal impact. TAYLRoACH is a low inertia, minimally actuated robot, and many variables, such as ground contact, roll, pitch, and leg position are not controlled during this experiment. This leads to variation among trials, shown in Fig. 5.2.

We break these data into three events: before tail actuation, during tail actuation, and after tail actuation. We find that each event has distinct characteristics.

As shown in figure 5.3, yaw rate is very high during tail actuation (mean 285$^\circ sec^{-1}$). Before tail actuation, mean yaw rate is near zero (-7$^\circ sec^{-1}$), suggesting the robot is going on average straight, although it is still subject to variation. After tail actuation, the average yaw rate is -41$^\circ sec^{-1}$. The difference in yaw rate before and after actuation (both periods in which the tail is unactuated and free) may be accounted for by the impact of the tail. This impact reduces the total turn angle of the robot and is undesired. Since these yaw rates are measured over different time periods, it is useful to look at the total yaw angle as well.

In Fig. 5.4 we see that the yaw displacement before actuation is small (-7°), while it is large during actuation (68°) and after actuation (-24°). The impact of the tail decreases the total turn of the robot, on average, by 35$\%$. Due to the large variation in results, feedback control is applied to

---

[1] www.naturalpoint.com/optitrack

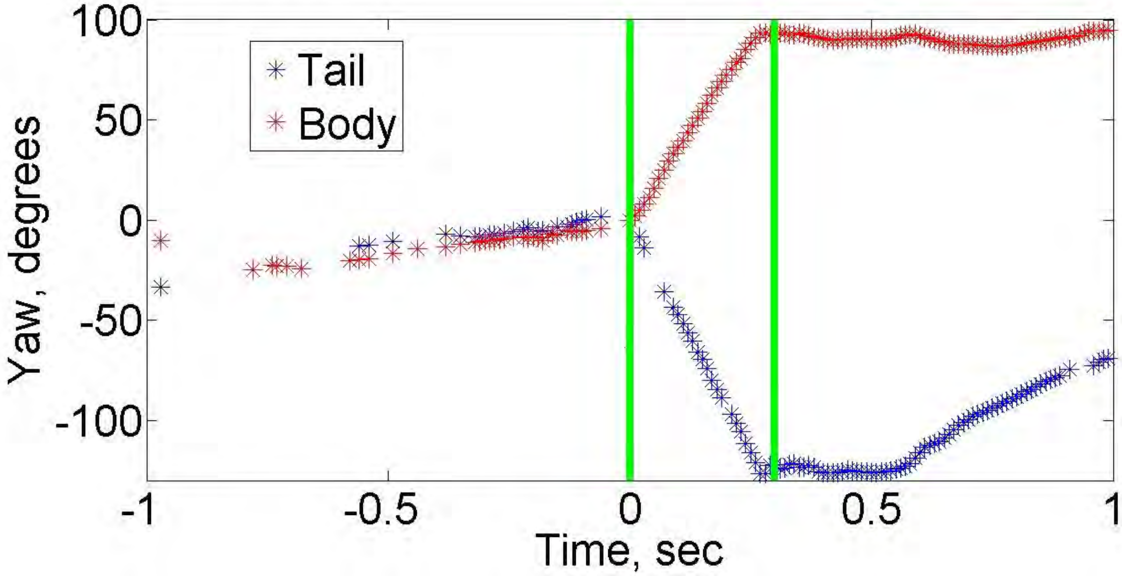

Figure 5.1: Data from an example trial showing the yaw displacement of the body and tail with respect to time. At the beginning of the trial the robot moves forward without any steering input. At the first vertical line, the tail is actuated. This actuation ends at the second vertical line while the robot continues running.

obtain more consistent turns.

5.2 Body Position Feedback Control

5.2.1 Body Angle Control using the Tail and Gyroscope Feedback

A tail control mode was implemented that produces a turn of the body very rapidly using feedback from the gyroscope. The body can be turned up to 90 degrees using this method, before the tail saturates. After tail saturation, the legs would have to be engaged to turn the robot further, or the tail would have to be reset so it can be actuated again.

Due to the varying ground contact friction, it is difficult to establish an input/output map of tail motion to body motion. Thus, a PID controller would be difficult to implement. Instead, a "bang-bang" controller was used, shown in Fig. 5.5, applying maximum torque to the tail unless the body is within five degrees of the goal angle. This serves as a deadband, and no torque is applied in this case. Using maximum torque ensures that the static friction is overcome and that the robot operates in the dynamic friction regime. This allows the robot to make turns of up to 90 degrees without the tail saturating, depending on the robot's forward speed. Using this gyro based control, the robot can make a controlled 90 degree turn in one quarter of a second, as shown in Figure 5.6.

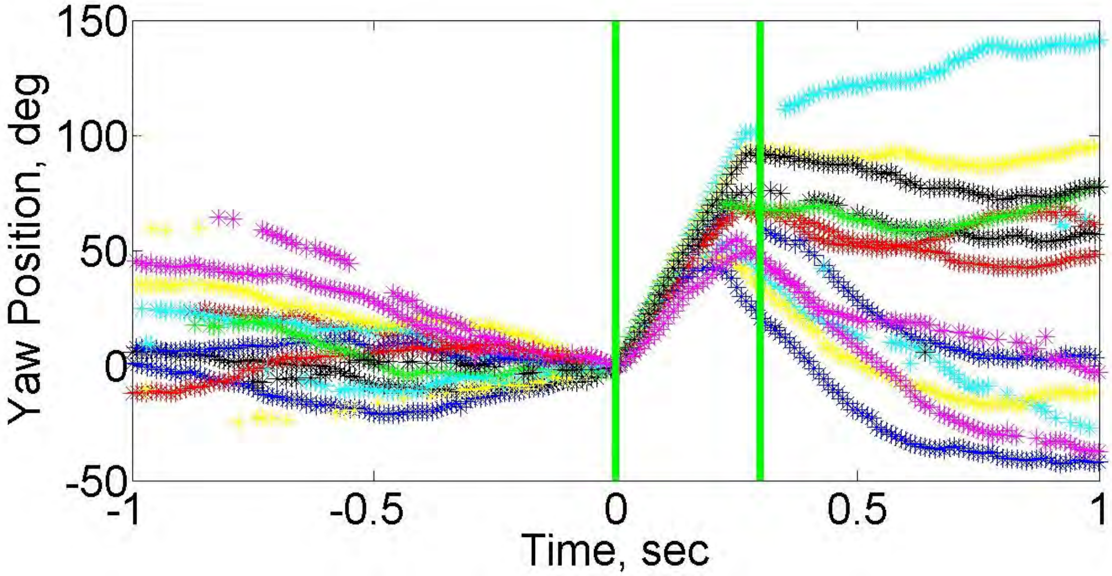

Figure 5.2: Body yaw vs. time. Fourteen trials were used to measure the variation in open loop turning. This plot is normalized so that at the point of tail actuation, time and body yaw are zero.

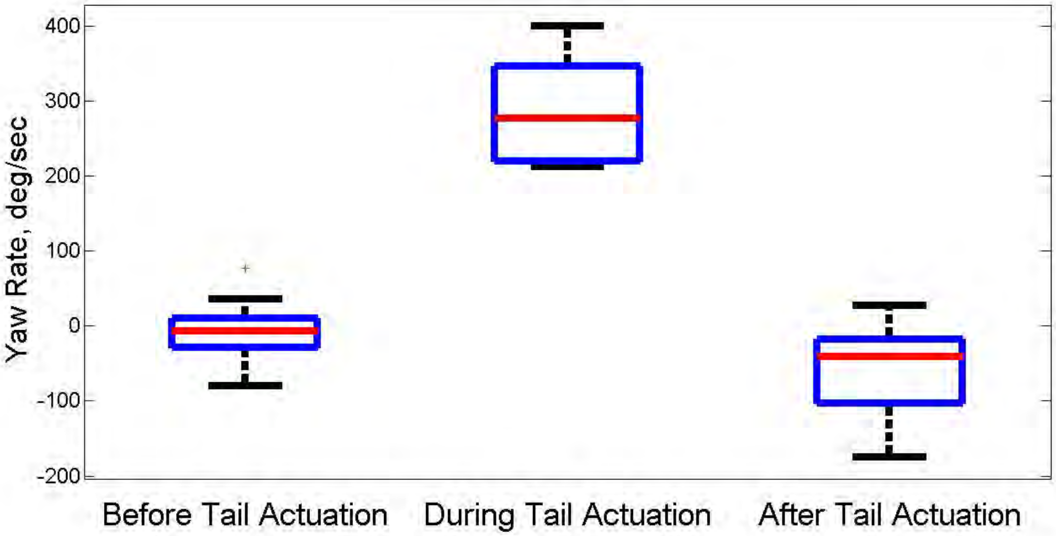

Figure 5.3: Body yaw rate, before, during, and after tail actuation. The red line marks the mean, the blue box marks one standard deviation, and the black bars mark minimum and maximum values. N = 14

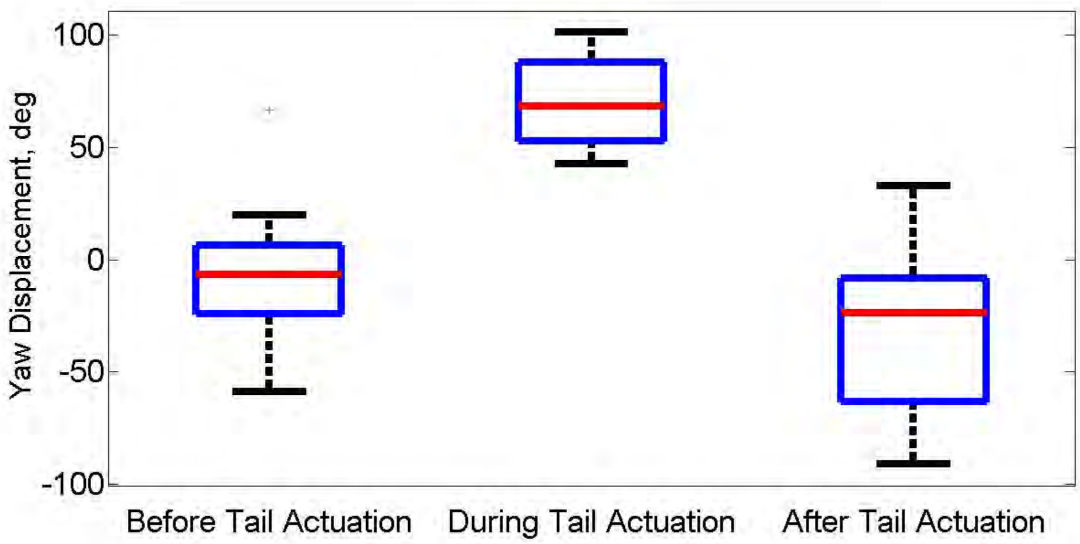

Figure 5.4: Mean, standard deviation, minimum, and maximum of yaw displacement, before, during, and after tail actuation. N = 14

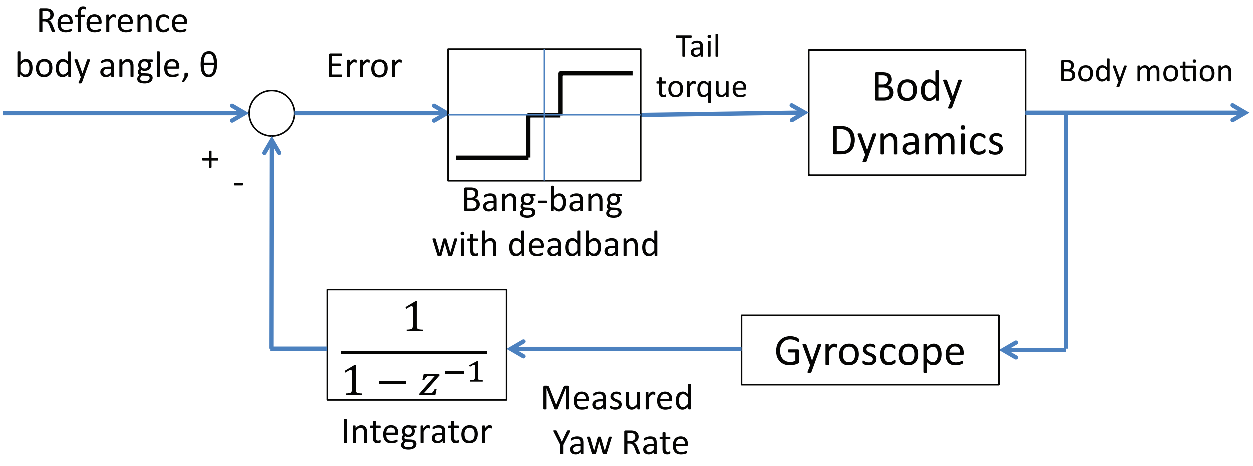

Figure 5.5: Control block diagram for the body angle control. The tail is given maximum positive or negative torque when away from the reference angle, and given zero torque in a small deadband to prevent unwanted high frequency actuation.

The bang-bang controller is able to remove much of the variation seen in open loop actuation. 10 trials each were performed as the robot was commanded to turn 30, 60, and 90°. As shown in Table 5.1, for 30 and 60° turns the RMS error is less than five degrees, the size of the control deadband. Control becomes more difficult at more extreme angles. At 90° the RMS error is over

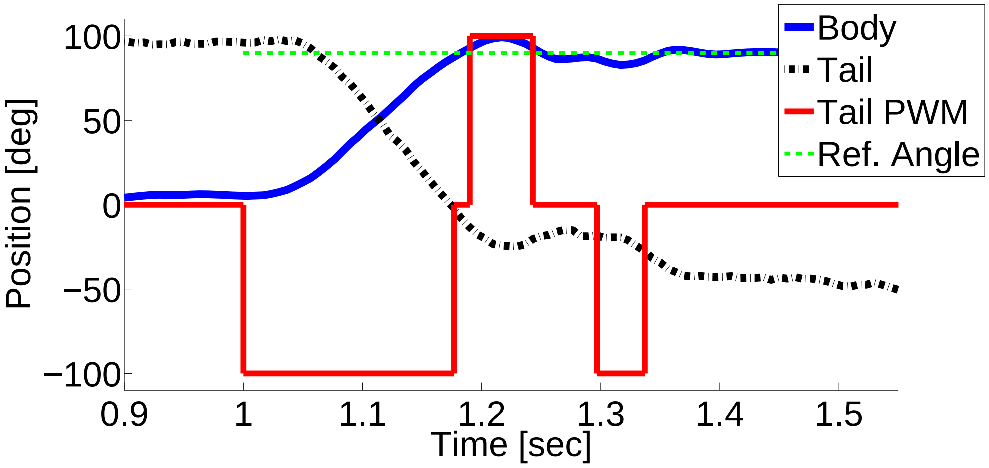

Figure 5.6: The tail motion induces a turn in the body. The bang-bang controller reacts to any overshoot by reversing the direction of the tail movement. A controlled 90 degree turn is performed in about 0.25 seconds.

13°. With high friction, the tail rotates more quickly relative to the body, meaning that the tail's range of motion may be consumed before reaching the target angle. If this occurs, an internal impact is created, turning the robot away from the target angle. This can lead to large errors, but an increased (or unlimited) range of motion would eliminate this problem. This occurred in a single trial, denoted by the black cross on Figure 5.7.

Table 5.1: RMS error and commanded angle.

Commanded Angle	RMS Error
30°	3.8°
60°	4.5°
90°	13.2°

5.2.2 Turning Radius

Figure 5.8 shows the robot position, heading, and speed while the closed loop tail control is actuated. The origin of the arrow is the robot position, the direction of the arrow is the robot's heading, and the length of the arrow is proportional to the robot's velocity. The robot is able to complete a 90 degree turn in a 4 cm space. Fig. 5.9 shows screenshots from a video detailing a controlled turn.

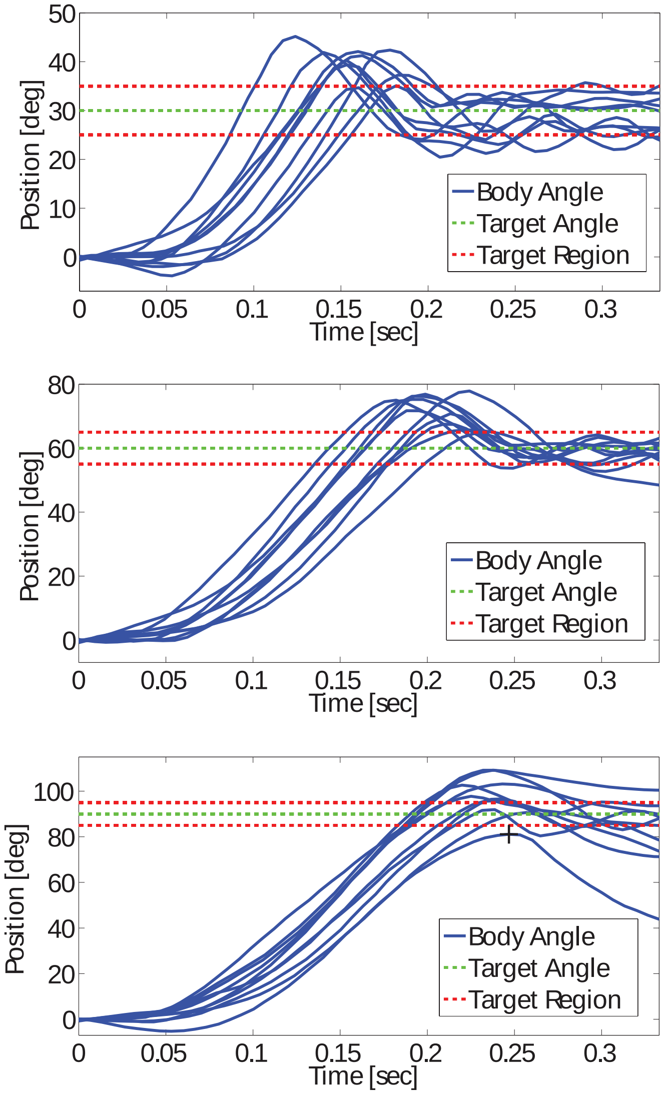

Figure 5.7: Results of the bang-bang controller commanded to 30, 60, and 90° turns. 10 trials for each target angle. The black cross shows where, in one trial, the tail reached the end of its range of motion, creating an internal impact and turning the robot away from the target angle.

5.2.3 Turning on a High Friction Surface using an Alternating Tripod Gait

SailRoACH is able to generate rapid turns using its sail as an inertial mechanism. Due to SailRoACH employing an alternating tripod gait unlike TAYLRoACH, it is able to turn on high friction surfaces as well. The alternating tripod gait causes periodic variation in the robot's normal forces [10], lowering the effective coefficient of friction, as discussed in Section 3.2.4. Fig. 5.10 shows the results of a controlled inertial turn performed on a high friction surface (carpet, $\mu_s \sim 2.0$).

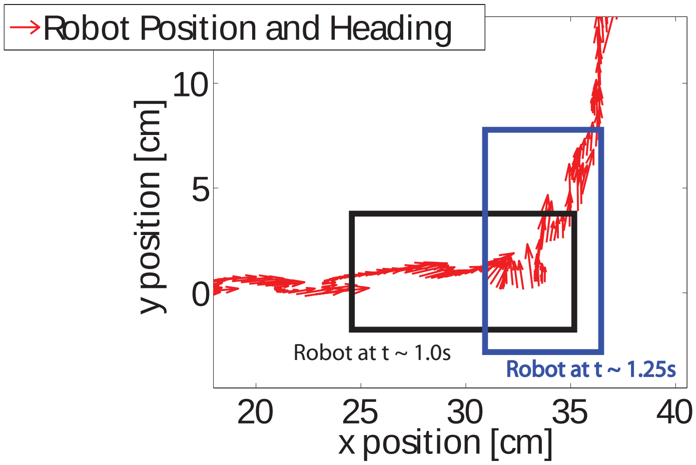

Figure 5.8: Data from a closed loop 90 degree inertial tail turn. The origin of the arrow is the robot position, the direction of the arrow is the robot's heading, and the length of the arrow is proportional to the robot's velocity. The robot makes a 90 degree turn in the space of approximately 4 cm, or 0.4 body lengths, without slowing down.

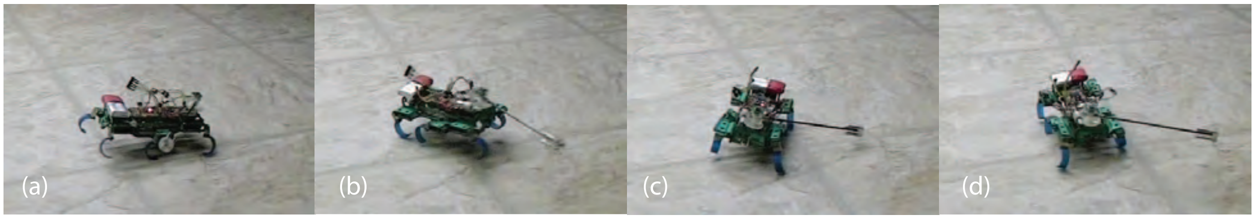

Figure 5.9: TAYLRoACH makes a controlled 90 degree turn on a tile surface. (a) Tail starts to move [t = 0.0s] (b) Robot about halfway through turn [t = 0.14s] (c) Robot overshoots 90° target [t = 0.23s] (d) Tail corrects overshoot, robot has made 90° turn [t = 0.30s]

SailRoACH is able to consistently make transient $200°sec^{-1}$ tail inertial turns on carpet, while running at 1.8 ms^{-1}. It should be noted that this turn is performed with the same actuator used for the aerodynamic steering.

5.3 Performance Characterization

To characterize the performance of the inertial tail closed loop control, we examine the step response data from Section 5.2.1. Neither the control law, nor the surface dynamics of the tile are linear, but we compare the performance of the controller to a linear second order system. The peak time and percent overshoot were measured for all trials. A delay of 50 ms is assumed, as this is the approximate time it takes from when the control command is issued to when the tail torque over-

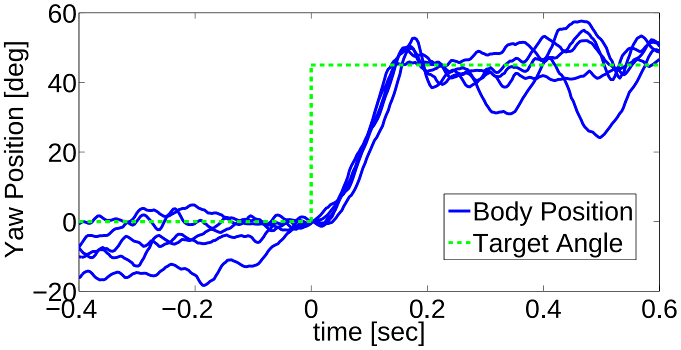

Figure 5.10: Heading of SailRoACH as a function of time during inertial turning. Before $t = 0$ no steering control is employed. At $t = 0$ a 45 degree turn is commanded using inertial exchange. SailRoACH makes a controlled 45 degree turn at approximately $200° sec^{-1}$ on carpet ($\mu \sim 2.0$).

comes the static friction torque. The calculated natural frequency and damping ratio are shown in Table 5.2. The data compared to its linear approximation are shown in Fig. 5.11.

Table 5.2: Performance Characterization.

Commanded Turn	Natural Freq. [Hz]	Damping Ratio
30°	5.02 ± 0.86	0.34 ± 0.098
60°	3.70 ± 0.31	0.47 ± 0.099

The linear second order step response does not serve as a model of the behavior, but does provide a sense of the performance capabilities of the system. For 30° turns, the robot turns with a natural frequency of 5 Hz, whereas for 60° turns, this is reduced to less than 4 Hz. This is likely due to the actuator saturation. The actuator can switch directions quickly but cannot move the body faster than about 525 $° sec^{-1}$.

5.4 Aerodynamic Turning

SailRoACH was run forward at a 21 Hz stride frequency for 60 strides with its sail held at constant position. As a control, the same experiments were done with the sail replaced by a ballast of the same weight but minimal aerodynamic properties (refer to Fig. 4.15). Results were recorded using a Vicon motion capture system. Eight to fourteen trials were performed for each configuration. When the robot first starts running, there is a transient phase where its heading changes due to the stochastic nature of the surface contact. All measurements of yaw rate and speed are made at steady state, and this transient effect is neglected. The paths described by the robot while running are shown in Fig. 5.14.

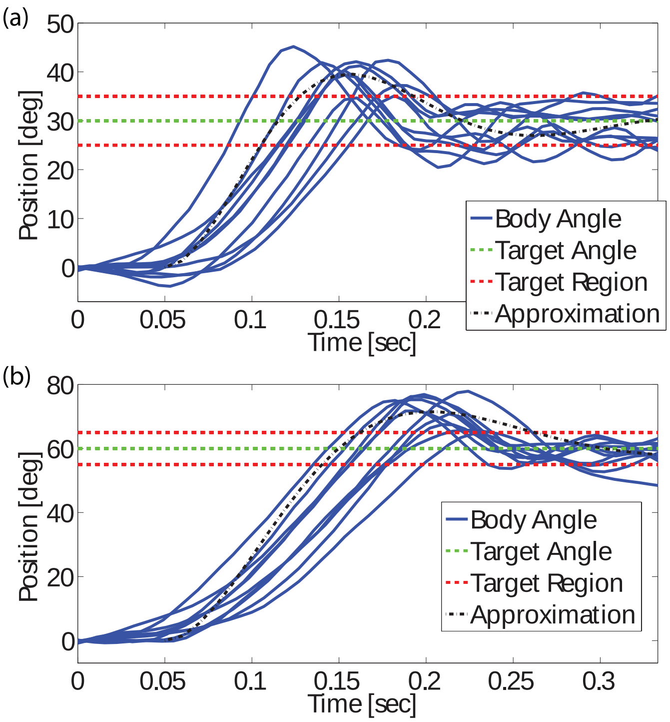

Figure 5.11: (a) For the 30 degree step resonse, the controller has performance similar to that of a second order linear system with a natural frequency of 5 Hz and a damping ratio of 0.34. (b) For the 60 degree step resonse, the controller has performance similar to that of a second order linear system with a natural frequency of 3.7 Hz and a damping ratio of 0.47. .

When equipped with the ballast, the center of mass is shifted, but aerodynamic effects are negligible. This does not significantly affect the path of the robot. The robot turns right slightly in many of these trials, irrespective of ballast position. This is likely due to a slight asymmetry in the robot's hand assembled structure.

When the sail is placed at an angle, the robot turns due to the aerodynamic torque on the body. With the sail 30 degrees left, the robot turns at an average of 51$^\circ sec^{-1}$ while running at steady state. When placed at 30 degrees right, the robot turns at an average of -73$^\circ sec^{-1}$. The ballast performs significantly worse, at 2$^\circ sec^{-1}$ and -25$^\circ sec^{-1}$ for left and right placement, respectively. These measurements can also be found in Table 5.3.

When the ballast is positioned at zero degrees (straight back), the turning rate is -15$^\circ sec^{-1}$, compared to 0$^\circ sec^{-1}$ when the sail is positioned at zero degrees. This indicates that the sail provides a stabilizing torque while the robot runs forward.

Table 5.3: Steady State Yaw Rate and Speed, 21 Hz Stride Freq.

Configuration	$\dot{\theta}$ [$^\circ sec^{-1}$]	Speed [ms^{-1}]
Sail Left	51 ± 19	2.02 ± 0.10
Ballast Left	2 ± 16	1.86 ± 0.12
Sail Center	0 ± 13	2.28 ± 0.05
Ballast Center	-15 ± 22	2.09 ± 0.05
Sail Right	-73 ± 23	1.84 ± 0.19
Ballast Right	-25 ± 19	1.99 ± 0.10
VelociRoACH [10]	–	∼2.0

5.4.1 Forward Speed

For maneuverability, maintaining high speed running is important. The sail mechanism constitutes 23% of the total robot weight, and adds aerodynamic drag, which may slow the robot down. Experimental evidence however, does not show this. When running forward with the sail or ballast at an angle, the steady state speed of the robot was between 1.84 and 2.02 ms^{-1}, as shown in Table 5.3. When the sail or ballast was positioned rearward, the sail produces slightly higher speeds, at 2.28 ms^{-1} versus 2.09 ms^{-1} for the ballast. This is mostly likely due to the stabilizing effect of the sail, which rejects yaw disturbances that may slow the robot down.

Haldane et al. [10] measured the speed of this robot chassis without an additional sail mechanism, and reported approximately 2 ms^{-1} at 21 Hz running frequency. The robot is not power limited, but limited by stability. The extra mass and aerodynamic stabilizing torque may ensure footfalls are more consistent and could explain this performance difference.

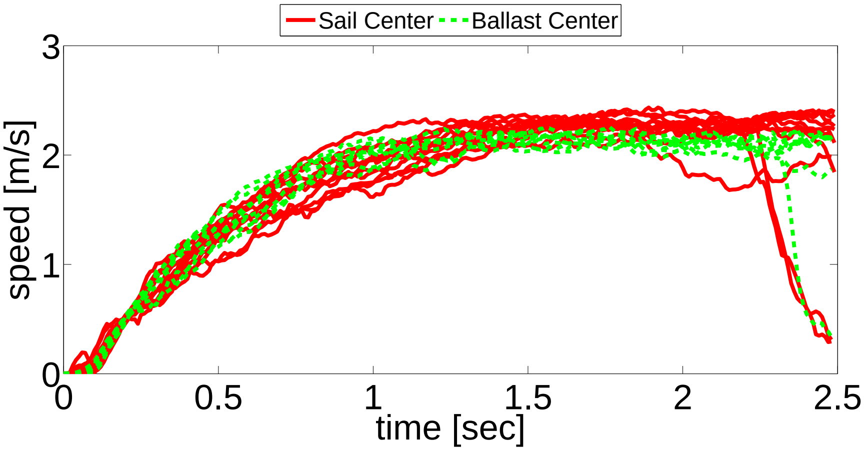

Figure 5.12: When the sail is centered, yaw disturbances are reduced due to an aerodynamic aligning torque, resulting in better forward speed performance.

5.5 Comparison to Other Turning Methods

Many methods have been demonstrated that allow legged robots to turn, but most employ the legs themselves to turn, and are ineffective at high speeds. Both inertial and aerodynamic tail turning do not affect leg gait, which can be advantageous. To examine the ability to turn while running at high speeds, McClung [31] defines a turning performance parameter:

$$K = \dot{\theta} v \tag{5.1}$$

where $\dot{\theta}$ and v are the simultaneous yaw rate and speed. We will use this to characterize various turning methods.

5.5.1 Differential Drive

The OctoRoACH [37] turns by moving legs on one side faster than the other. This causes the outside of the robot to move farther than the inside, producing a turn. The OctoRoACH is able to make 90$^\circ sec^{-1}$ turns while running forward at 0.4 ms^{-1}. This turning method is effective, but precludes high speed running. The leg sides are not in phase with each other, an alternating tripod gait cannot be used, and the force produced by the legs cannot be coordinated, limiting the top speed.

Closed loop inertial turning with tail actuation is both precise and rapid, and makes sharper turns in shorter time compared with differential drive, or other methods. Figure 5.13 shows the path the TAYLRoACH II takes while executing a 90 degree turn. Three methods are used to make the turn. The first method employs differential drive steering (which, due to its similar layout to OctoRoACH, it is capable of) with gyroscope feedback. Using this method TAYLRoACH can accurately turn 90 degrees, but the path required is much larger and the time required is three times greater than using inertial turning. The second method used is by actuating the tail without feedback. This results in a quick, sharp, but inaccurate turn. Finally, the robot is turned using the tail with gyroscope feedback. Using this method, a 90 degree turn is achieved in 1/3 of a second with a turning radius of 4 cm.

5.5.2 Differential Leg Phasing

The XRL robot uses differential leg phasing and a modified Buehler clock to turn [33]. This mode has the advantage of maintaining an alternating tripod gait, but requires a high degree of intra-stride control, and uses 6 motors. It is possible that using two motors could also accomplish similar behavior. As shown in [33], the XRL can turn at 8$^\circ sec^{-1}$while running forward at 0.18 ms^{-1}.

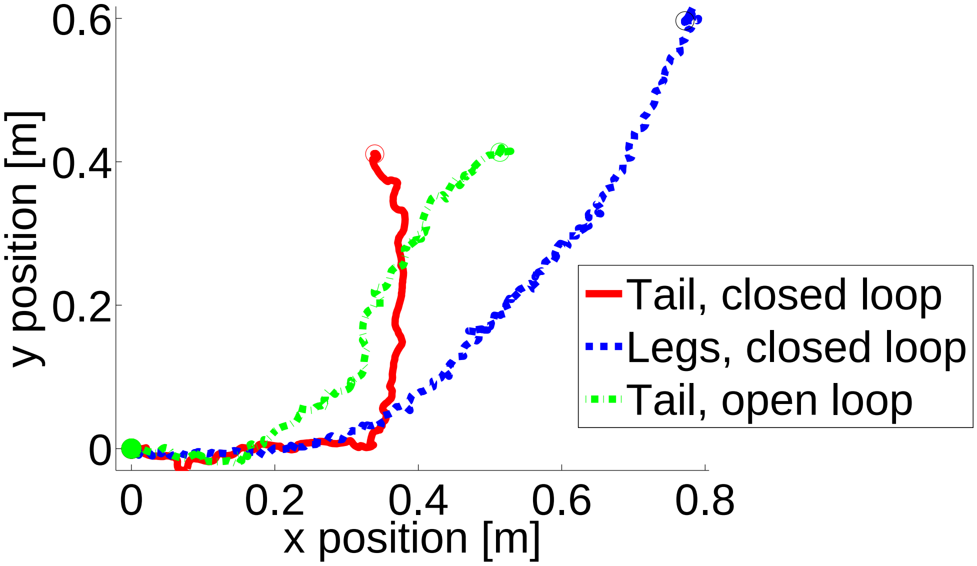

Figure 5.13: Path of the robot as it runs forward, executes a 90 degree turn, and runs forward again. Turns performed on tile surface.

5.5.3 Modified Leg Kinematics

The SPRAWL family of robots turns effectively while running forward. iSprawl is a hexapedal robot that can change the angle of its middle legs. This causes a yaw moment, turning the robot. At 6Hz stride frequency, iSprawl is able to run forward at 0.5 ms^{-1}while turning at approximately 40°sec^{-1}[31].

5.5.4 Inertial Turning

TAYLRoACH [24] is able to turn rapidly on low friction surfaces using a tail to induce a quick exchange of angular momentum, as discussed in Section 5.2.1. This generates a yaw rate of 360°sec^{-1} while running forward at 0.3 ms^{-1}.

5.5.5 Aerodynamic Turning

SailRoACH is able to use its sail to generate torques aerodynamically, turning the robot. This turning method is completely decoupled from the legs, meaning an alternating tripod gait can be maintained. Although not as rapid as the inertial turning method, aerodynamic turning can be executed continuously, as long as forward speed is maintained, unlike inertial turning, which requires rapid actuation of a mass and generally takes place only over a short period of time.

5.5.6 Maneuverability Comparison

Table 5.4 shows the maneuverability, K, of each highlighted robot. Many different methods of turning are effective, but aerodynamic and inertial turning allow for high yaw rates and for an alternating tripod gait to be employed, making the product of yaw rate and forward velocity high.

Table 5.4: Comparison of Turning Methods.

Robot	$\dot{\theta}$ [$^\circ sec^{-1}$]	$K = \dot{\theta} v$ [$^\circ ms^{-2}$]	Transient?
OctoRoACH [37]	90	36	No
DASH [2]	50	25	No
XRL [33]	8	1.44	No
iSprawl [31]	40	18	No
TAYLRoACH (Inertial, low μ)	360	108	Yes
SailRoACH (Inertial, high μ)	200	360	Yes
SailRoACH (Aerodynamic)	70	134	No

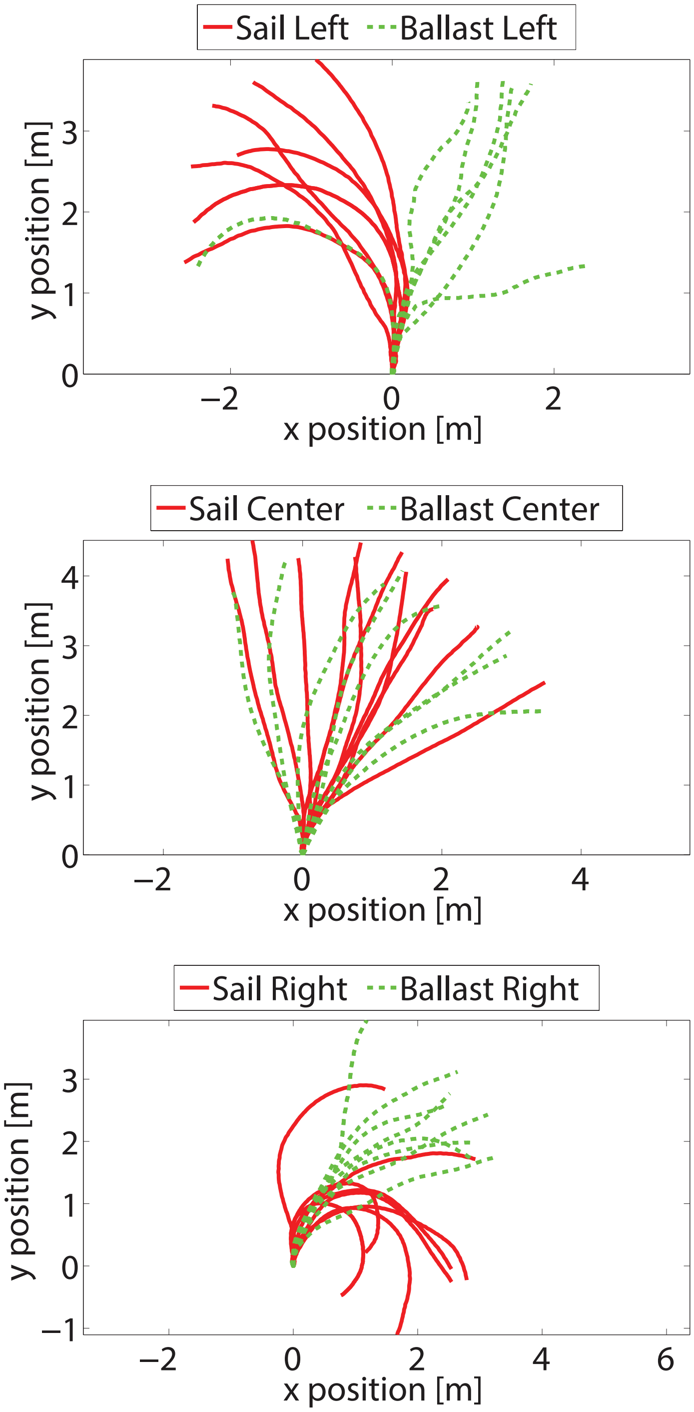

Figure 5.14: (a) The paths of the robot when the sail or ballast is held 30 degrees to the left of center. (b) The paths of the robot when the sail or ballast is held at center. (c) The paths of the robot when the sail or ballast is held 30 degrees to the right of center. Placing the sail at an angle produces a turning moment, while placing the sail directly behind the robot produces a stabilizing moment.

Chapter 6

Conclusion

6.1 Summary

This work has presented two novel ways to induce turning in legged robots. Previous work surrounding turning and tail use in robots and animals was reviewed in Chapter 2. Chapter 3 presented models of inertial and aerodynamic steering, which can be used to predict performance and inform design. This chapter also discussed scaling laws that can help us understand how different methods of turning can be best applied across a wide array of robot morphologies. Chapter 4 detailed the design and software of the tail and sail mechanisms, and also provided a powertrain analysis.

Chapter 5 reviewed experiments performed with the robot platforms, demonstrating rapid, low radius, precise turning in the inertial turning case, and turning during high speed running for the aerodynamic turning case. Additionally, a comparison of these turning methods to other common legged robot turning methods was made.

6.2 Future Work

6.2.1 Inertial Turning

The inertial tail turning presented here mostly focuses on two surfaces, tile and carpet. Surface variability, and its interaction with the robot's duty factor, is a rich area for exploration. A robot with a low duty factor (and therefore large airborne phase) may be able to turn on extremely high friction surfaces, or even surfaces where normal or constraint forces may be an issue, such as a rock bed. Another issue yet to be explored is timing the actuation of the tail with a specific leg phase. It may be that by optimizing when the tail actuates relative to the leg phase (and thus normal force on the robot), better performance could be produced. It should be noted that this was not examined due to issues of timing. The motor can take up to 50 milliseconds to develop significant torque, but a full leg stride at 24 Hz only lasts 42 milliseconds.

Other avenues for exploration would include powertrain optimization and a more through examination of the effect of initial tail position. Developing better models of leg compliance could inform a better friction model, which could be used to improve the design and thus performance of the robot-tail system greatly.

6.2.2 Aerodynamic Turning

In this work, aerodynamic turning is performed using a flat plate surface. This surface is in no way optimal and could be greatly improved. A higher performing airfoil would produce higher yaw rates at lower forward speeds. Additionally, the aerodynamic turning demonstrated here is done open loop, with the flat plate held at a constant position. Implementing a closed loop controller with gyroscope or other sensor feedback could ensure a constant yaw rate, or turning radius. Integrating this controller with the legged turning, and feedback from a camera or other navigational sensor, would allow for path-following behavior at high speeds that may not be possible with legged control only.

The sail is generally held behind the robot as the default position. This is useful because the aerodynamic torque stabilizes the yaw of the robot. If the default sail position were directly in front of the robot, the robot would be unstable to yaw disturbances while running at high speeds, but may also be more responsive. A closed loop controller may be able to stabilize the robot and allow for high performance maneuvers that would not be possible with a rear facing tail.

Another avenue for improvement would be to use the aerodynamic and inertial turning together. This was not fully explored in this work, but if the tail is actuated rapidly while the robot runs forward at high speeds, this could have a dramatic effect on the sail speed and thus the aerodynamic torque on the robot. It should be noted that, depending on the tail position and velocity, the inertial and aerodynamic torques could be in similar or opposite directions. This brings up interesting questions about controllability and reachability of the system that could be addressed in future work.

Aerodynamic turning could have other benefits, unrelated to performance. It is difficult to introduce a constant yaw disturbance to a robotic system, but this may be desirable to study legged locomotion. Since the speed of the robot at steady state is fairly constant, and the aerodynamic torque is proportional to speed squared, this may provide a way to systematically test the stability margins of a legged robot.

Bibliography

[1] P. Birkmeyer, A. G. Gillies, and R. S. Fearing. CLASH: Climbing vertical loose cloth. In *IEEE Int. Conf. on Intelligent Robots and Systems (IROS)*, pages 5087–5093. IEEE, 2011.

[2] P. Birkmeyer, K. Peterson, and R. S. Fearing. DASH: A dynamic 16g hexapedal robot. In *IEEE Int. Conf. on Intelligent Robots and Systems*, St. Louis, MO, 2009.

[3] Paul Birkmeyer, Andrew G. Gillies, and Ronald S. Fearing. Dynamic climbing of near-vertical smooth surfaces. In *IEEE/RSJ Int. Conf. on Intelligent Robots and Systems*, pages 286–292, 2012.

[4] E. Chang-Siu, T. Libby, M. Tomizuka, and R.J. Full. A lizard-inspired active tail enables rapid maneuvers and dynamic stabilization in a terrestrial robot. In *IEEE Int. Conf. on Intelligent Robots and Systems*, September 2011.

[5] Jonathan E. Clark, Daniel I. Goldman, Pei-Chun Lin, Goran Lynch, Tao S. Chen, Haldun Komsuoglu, Robert J. Full, and Daniel Koditschek. Design of a bio-inspired dynamical vertical climbing robot. In *Robotics Science and Systems*, 2007.

[6] S.J.J.F. Davies and M. Bamford. *Ratites and Tinamous: Tinamidae, Rheidae, Dromaiidae, Casuariidae, Apterygidae, Struthionidae*. Number v. 7; v. 9 in Bird Families of the World. Oxford University Press, 2002.

[7] V. Dürr and W. Ebeling. The behavioural transition from straight to curve walking: kinetics of leg movement parameters and the initiation of turning. *Journal of Experimental Biology*, 208(12):2237–2252, 2005.

[8] J.P. Dyhr, T.L. Daniel, K.A. Morgansen, and N.J. Cowan. Flexible strategies for flight control: an active role for the abdomen. *J. Exp. Biol., in prep*.

[9] R.S. Fearing. Challenges for effective millirobots. In *Int. Symp. on. Micro-NanoMechatronics and Human Science*, November 2006.

[10] D. Haldane, K. Peterson, F. Garcia Bermudez, and R.S. Fearing. Animal-inspired design and aerodynamic stabilization of a hexapedal millirobot”. In *IEEE Int. Conf. on Robotics and Automation*, May 2013.

[11] K. Hirata, T. Takimoto, and K. Tamura. Study on turning performance of a fish robot. *First International Symposium on Aqua Bio-Mechanisms*, 2002.

[12] A. M. Hoover and R. S. Fearing. Fast scale prototyping for folded millirobots. In *IEEE Int. Conf. on Robotics and Automation*, Pasadena, CA, 2008.

[13] A. M. Hoover, E. Steltz, and R. S. Fearing. Roach: An autonomous 2.4g crawling hexapod robot. In *IEEE Int. Conf. on Intelligent Robots and Systems*, Nice, France, Sept. 2008.

[14] A.M. Hoover, S. Burden, X-Y. Fu, S.S. Sastry, and R.S. Fearing. Bio-inspired design and dynamic maneuverability of a minimally actuated six-legged robot. In *IEEE International Conference on Biomedical Robotics and Biomechatronics. BioRob 2010.*, Sep. 2010.

[15] J. Hoyo, A. Elliott, and J. Sargatal. *Handbook of the Birds of the World: Barn-owls to hummingbirds*. Handbook of the Birds of the World. Lynx Edicions, 1999.

[16] Ian W Hunter, John M Hollerbach, and John Ballantyne. A comparative analysis of actuator technologies for robotics. *Robotics Review*, 2, 1991.

[17] D.L. Jindrich and R.J. Full. Many-legged maneuverability: dynamics of turning in hexapods. *J Exp Biol*, 202(12):1603–1623, 1999.

[18] A.M. Johnson, T. Libby, E. Chang-Siu, M. Tomizuka, R.J. Full, and D.E. Koditschek. Tail assisted dynamic self righting. In *15th International Conference on Climbing and Walking Robots and the Supporting Technologies for Mobile Machines*, July 2012.

[19] A. Jusufi, D.I. Goldman, S. Revzen, and R.J. Full. Active tails enhance arboreal acrobatics in geckos. *Proceedings of the National Academy of Sciences*, 105(11):4215–4219, 2008.

[20] A Jusufi, D T Kawano, T Libby, and R J Full. Righting and turning in mid-air using appendage inertia: reptile tails, analytical models and bio-inspired robots. *Bioinspiration & Biomimetics*, 5(4):045001, 2010.

[21] S. Kim, A. T. Asbeck, M. R. Cutkosky, and W. R. Provancher. Spinybotii: Climbing hard walls with compliant microspines. In *12th Intl Conf on Advanced Robotics*, pages 601–606, 2005.

[22] Sangbae Kim, M. Spenko, S. Trujillo, B. Heyneman, V. Mattoli, and M.R. Cutkosky. Whole body adhesion: hierarchical, directional and distributed control of adhesive forces for a climbing robot. In *IEEE Int. Conf. on Robotics and Automation*, pages 1268–1273, Rome, Italy, 2007.

[23] N.J. Kohut, A.M. Hoover, K.Y. Ma, S.S. Baek, and R.S. Fearing. Medic: A legged millirobot utilizing novel obstacle traversal. In *IEEE Int. Conf. on Robotics and Automation*, May 2011.

[24] N.J. Kohut, A.O. Pullin, D.W. Haldane, D. Zarrouk, and R.S. Fearing. Precise dynamic turning of a 10 cm legged robot on a low friction surface using a tail. In *IEEE Int. Conf. on Robotics and Automation*, May 2013.

[25] N.J. Kohut, D. Zarrouk, K.C. Peterson, and R.S. Fearing. Aerodynamic steering of a 10 cm high-speed running robot. Submitted, 2013.

[26] Mirko Kovac, Wassim Hraiz, O. Fauria, J.C. Zufferey, and Dario Floreano. The EPFL jumpglider: A hybrid jumping and gliding robot with rigid or folding wings. In *IEEE Int. Conf. on Robotics and Biomimetics (ROBIO)*, pages 1503–1508, 2011.

[27] David Lentink, Stefan R. Jongerius, and Nancy L. Bradshaw. The scalable design of flapping micro-air vehicles inspired by insect flight. *Flying Insects and Robots, edited by D. Floreano, M. Srinivasan, C. Ellington, and J.C. Zuffrey*, page 185, 2009.

[28] T. Libby, V. Gudenus, P. Harrington, and R.J. Full. Coordination between inertial and impulsive mechanisms during rapid turns in lizards. In *Society for Integrative and Comparative Biology Annual Meeting*, January 2013.

[29] T. Libby, T.Y. Moore, E. Chang-Siu, D. Li, D.J. Cohen, A. Jusufi, and R.J. Full. Tail-assisted pitch control in lizards, robots and dinosaurs. *Nature*, 481:181–184, 2012.

[30] G. A. Lynch, J.E. Clark, P.C. Lin, and D.E. Koditschek. A bioinspired dynamical vertical climbing robot. *International Journal of Robotics Research*, 31:974–976, 2012.

[31] A.J. McClung. *Techniques for dynamic maneuvering of hexapedal legged robots*. PhD thesis, Stanford University, 2006.

[32] C. Nie, S.C. Van Dooren, J. Shah, and M. Spenko. Execution of dynamic maneuvers for unmanned ground vehicles using variable internal inertial properties. In *IEEE Int. Conf. on Intelligent Robots and Systems (IROS)*, pages 4226–4231. IEEE, 2009.

[33] C. Ordonez, N. Gupta, E.G. Collins Jr., and J.E. Clark. Power modeling of the XRL hexapedal robot and its application to energy efficient motion planning. In *15th International Conference on Climbing and Walking Robots and the Supporting Technologies for Mobile Machines*, July 2012.

[34] I. Penskiy, P. Samuel, J.S. Humbert, and S. Bergbreiter. A bio-inspired active tail control actuator for nano air vehicles. In *IEEE Int. Conf. on Robotics and Automation (ICRA)*, pages 4635–4640. IEEE, 2012.

[35] K. Peterson, P. Birkmeyer, R. Dudley, and R.S. Fearing. A wing-assisted running robot and implications for avian flight evolution. *Bioinspiration & Biomimetics*, 6(4):046008, 2011.

[36] W.R. Provancher, S.I. Jensen-Segal, and M.A. Fehlberg. Rocr: An energy-efficient dynamic wall-climbing robot. *Mechatronics, IEEE/ASME Transactions on*, 16(5):897 –906, Oct. 2011.

[37] A.O. Pullin, N.J. Kohut, D. Zarrouk, and R.S. Fearing. Dynamic turning of 13 cm robot comparing tail and differential drive. In *IEEE Int. Conf. on Robotics and Automation*, May 2012.

[38] A. Quaranta, M. Siniscalchi, and G. Vallortigara. Asymmetric tail-wagging responses by dogs to different emotive stimuli. *Current biology: CB*, 17(6):R199, 2007.

[39] A. Schneider, J. Paskarbeit, M. Schaeffersmann, and J. Schmitz. Hector, a new hexapod robot platform with increased mobility-control approach. In *Advances in Autonomous Mini Robots: Proceedings of the 6-th AMiRE Symposium*, page 249. Springer, 2012.

[40] M. Spenko, G.C. Haynes, J.A. Saunders, M.R. Cutkosky, A.A. Rizzi, R.J. Full, and D.E. Koditschek. Biologically inspired climbing with a hexapedal robot. *Journal of Field Robotics*, 25:223 –242, 2008.

[41] C.H. Tyndale-Biscoe. *Life of Marsupials*. Contemporary biology. CSIRO, 2005.

[42] Evan R. Ulrich, Darryll J. Pines, and J. Sean Humbert. From falling to flying: the path to powered flight of a robotic samara nano air vehicle. *Bioinspiration & Biomimetics*, 5(4):045009, 2010.

[43] Rebecca M. Walter. Kinematics of 90° running turns in wild mice. *Journal of Experimental Biology*, 206(10):1739–1749, 2003.

[44] Rebecca M. Walter and David R. Carrier. Scaling of rotational inertia in murine rodents and two species of lizard. *Journal of Experimental Biology*, 205(14):2135–2141, 2002.

[45] R. J. Wood. The first takeoff of a biologically inspired at-scale robotic insect. *IEEE Trans. Robotics*, 24(2):341–347, April 2008.

[46] K. Yamafuji, T. Kawmura, and M. Feng. Elucidation of twisting motion of a falling cat and realization of cat-turn motion by a robot. In *International Symposium on Robotics*, volume 30, October 2004.

[47] D. Zarrouk and R.S. Fearing. Cost of transport of a dynamic hexapedal robot. In *IEEE Int. Conf. on Robotics and Automation*, May 2013.